# Time-of-day defines the efficacy of $NAD^+$ to treat diet-induced metabolic disease by adjusting oscillations of the hepatic circadian clock

Escalante-Covarrubias, Q[1]; Mendoza-Viveros, L[1,2]; González-Suárez, M[1]; Becerril-Pérez, F[1]; Pacheco-Bernal, I[1]; Carreño-Vázquez, E[2]; Mass-Sánchez, P[1]; Bustamante-Zepeda, M[1]; Orozco-Solís, R[2]; Aguilar-Arnal, L[1]*.

[1] Departamento de Biología Celular y Fisiología, Instituto de Investigaciones Biomédicas, Universidad Nacional Autónoma de México, 04510 Mexico City, Mexico

[2] Laboratorio de Cronobiología y Metabolismo, Instituto Nacional de Medicina Genómica, 14610 Mexico City, Mexico

* To whom correspondence should be addressed: loreaguilararnal@iibiomedicas.unam.mx

## SUMMARY

The circadian clock is a time-tracking endogenous system which anticipates and coordinates adaptation to daily environmental fluctuations. Circadian misalignment leads to obesity, which is accompanied by reduced levels of the clock-controlled metabolite $NAD^+$. Concomitantly, increasing $NAD^+$ levels is emerging as a therapy for diet-induced obesity and type 2 diabetes; however, the impact of daily fluctuations of $NAD^+$ on these therapies remains unknown. Here, we demonstrate that time-of-day determines the efficacy of $NAD^+$ as a therapy for diet-induced metabolic disease in mice. Restoring regular $NAD^+$ oscillations at the onset of the active phase ameliorates metabolic markers of disease such as body weight and glucose and insulin tolerance, and restores hepatic gene expression related to inflammatory response and lipid metabolism. However, the same treatment designed to increase $NAD^+$ at the onset of the rest phase severely compromises these beneficial responses. Notably, hepatic nutrient-sensing mTOR, AMPK or AKT signaling, became rhythmic specifically in obese mice treated just before the active phase. Remarkably, $NAD^+$ at the onset of the rest phase was accompanied by uncoupled oscillations between the SCN and the hepatic clock, which were phase inverted in the liver, while keeping behavioral rhythms largely intact. These findings demonstrate that the time of day determines the beneficial effects of $NAD^+$-based therapies and pave the way for the basic strategy of a chronobiology-based therapeutic approach.


**Key words:** Circadian rhythms, obesity, $NAD^+$, chronotherapy, fatty acid oxidation, fatty liver disease, glucose homeostasis, transcriptomics.

## INTRODUCTION

In the last few decades, the prevalence of obesity has become epidemic through the world and is a major risk factor for type 2 diabetes (T2D)[1]. The main cause appears as combined inappropriate nutrition and sedentary lifestyles. Overweight, insulin resistance, β-cell dysfunction, increased circulating glucose and lipids and non-alcoholic fatty liver disease (NAFLD) characterize the pathophysiology of T2D[2]. Countless research efforts have explored pharmacological treatments for T2D and associated pathologies leading to promising compounds, which together with lifestyle interventions constitute first-line treatments[3]. During the last few years, the circadian system has been increasingly recognized as a key actor for development and treatment of diet-induced metabolic dysfunction. Yet, circadian rhythms in the clinical practice remain largely overlooked and time-of-day is hardly considered in treatment decisions[4-8].

Circadian rhythms are evolutionary conserved 24-hour cycles in physiology dictated by an intrinsic circadian clock. In mammals, the suprachiasmatic nucleus (SCN), a master timekeeper in the hypothalamus, receives photic cues from the retina to align internal and external time. The SCN distally synchronizes ancillary oscillators in peripheral tissues. Importantly, certain cues such as nutritional inputs effectively synchronize peripheral clocks[9]. Aligned synchrony between all body clocks maintains homeostasis and health, for example, by adjusting metabolic performance to daily environmental fluctuations. Conversely, persistent circadian misalignment is a cause of severe diseases, including obesity and metabolic syndrome, T2D or cardiovascular disease, amongst others[10-12]. At the molecular level, the circadian machinery is expressed in almost all cell types and consists of transcriptional-translational autoregulatory feedback loops. The positive loop is driven by the CLOCK:BMAL1

transcriptional activator, which rhythmically binds to E-box genomic elements, thereby activating transcription of many genes including the circadian repressors, Period (*Per1-3*) and Cryptochrome (*Cry1-2*). PER:CRY complexes directly repress CLOCK:BMAL1 leading to transcriptional silencing. A number of interlocked regulatory loops, such as the one governed by RORs/REV-ERBα to regulate *Bmal1* expression, intertwine to confer complexity, redundancy and robustness to circadian rhythms[13]. Consequently, a set of clock-controlled genes (CCGs) ranging from 5-25% depending on the tissue or cell type, display transcriptional circadian rhythms[14]. Notably, rhythmic transcripts are functionally related, including rate-limiting enzymes, hence providing means to adjust the pace of many metabolic pathways around the day and driving rhythms in the tissue metabolome[15-18]. A paradigmatic example is illustrated by daily rhythms in nicotinamide adenine dinucleotide ($NAD^+$) bioavailability, imposed by circadian oscillations in the clock-controlled gene *Nampt*, the rate limiting enzyme for the NAM salvage pathway to $NAD^+$[19,20]. Several lines of evidence demonstrate that the molecular clock and $NAD^+$ oscillations sustain mitochondrial function and bioenergetics, manifested in daily rhythms in respiration, fatty acid oxidation or nutrient utilization [21-25]. Indeed, it is considered that clock-controlled $NAD^+$ biosynthesis occupies a fundamental position connecting circadian metabolic pathways[26-28].

$NAD^+$ and its phosphorylated and reduced forms NADH, $NADP^+$ and NADPH, are coenzymes for hydride transfer enzymes, crucial to biological redox reactions. $NAD^+$/NADH ratio is a basic determinant of the rate of catabolism and energy production[29,30]. In fed state or nutrient overload $NAD^+$/NADH ratio falls, and a prolonged redox imbalance potentially leads to metabolic pathologies, such as diabetes[31]. Along these lines, extensive research demonstrates that $NAD^+$ levels significantly decline in metabolic tissues of obese mice and humans[32-37].

$NAD^+$ decay itself may contribute to metabolic dysfunction by distinct mechanisms, including increased oxidative stress and ROS production, disbalance in the oxidative-reductive capacity, disrupted $Ca^{2+}$ homeostasis, or reduced activity of sirtuins[38,39]; a class of deacetylase enzymes using $NAD^+$ as cofactor and known to influence mitochondrial function and metabolism. In recent years, $NAD^+$ has emerged as a target for the treatment of metabolic diseases, as boosting endogenous $NAD^+$ levels has been proven effective against diet-induced metabolic pathologies, including insulin resistance, hyperglycemia, hypertriglyceridemia and NAFLD[32,33,35,36,40-45]. All these studies aim to increase $NAD^+$ levels either genetically or pharmacologically, yet they mostly overlook the circadian trait of $NAD^+$ bioavailability. Consequently, the implications of circadian rhythms in the function and effectiveness of $NAD^+$ boosters as a therapy for diet-induced metabolic disfunction remain largely obscure.

In this work, we aimed to characterize the metabolic consequences of rhythms in $NAD^+$ levels. To approach this question, we used a mouse model of diet-induced obesity (DIO), which is known to present decreased, non-rhythmic levels of $NAD^+$ [15-17], and pharmacologically recovered daily rhythms of $NAD^+$ with a peak at the onset of the active phase. To do so, we used a daily timed intraperitoneal (IP) injection with $NAD^+$ itself at ZT11. We show that obese mice with enforced $NAD^+$ oscillations improved metabolic health, significantly lost weight, and corrected NAFLD. Our analyses revealed that hepatic transcriptional signatures of inflammation disappeared in these mice. Indeed, hepatic signaling involving AMPK, AKT, mTOR was rewired after restoring rhythmic $NAD^+$ in obese mice, providing increased insulin sensitivity during the active period. Together, we demonstrated that a single daily injection with $NAD^+$ treats the pathophysiology of diet-induced obesity, with comparable efficiency to $NAD^+$ precursors. Remarkably, these metabolic and molecular improvements were not recapitulated

by obese mice with antiphase increase of $NAD^+$, at the onset of the rest phase, which showed only mild recovery of metabolic health. Further analyses demonstrated that lipid oxidative pathways and the molecular clock are central mediators for phase-dependent, differential effects of $NAD^+$. Particularly, $NAD^+$ provided at the onset of the rest phase uncoupled oscillations between central and peripheral clocks, while food intake remained rhythmic. These findings reveal that timed $NAD^+$ supply can shape the oscillatory phase of the hepatic molecular clock *in vivo* and expose a previously unappreciated time-dependent effect of $NAD^+$ as a treatment for metabolic dysfunction, paving the way for chronotherapy and personalized medicine.

## RESULTS

### A timed treatment with $NAD^+$ reverses the metabolic phenotype of diet-induced obesity.

To understand whether daily $NAD^+$ administration improves metabolic fitness in obesity, we used a mouse model of diet-induced obesity (DIO) where instead of increasing $NAD^+$ by chronic supplementation with metabolic precursors, we directly supplied the metabolite itself in a daily single IP injection scheduled at ZT11, corresponding to an hour before the normal circadian rise of hepatic $NAD^+$ [16,17,21,27,46]. Hence, after 8 weeks of high-fat diet (HFD) feeding, mice were treated for 22 days with saline solution (HF group) or 50 mg/Kg of $NAD^+$ (HFN group, Figure S1A, see Methods section), at ZT11 (Figure 1A). Mice fed a chow diet were included as a control (CD group).

At week 8 on HFD, mice displayed expected increase in body weight which was accompanied by significantly higher caloric intake during both light and dark periods [47] (Figure 1B, S1B, S1C,

S1D). Notably, after 14 days of $NAD^+$ chronotherapy, a significant decrease in total body weight was observed in obese treated mice (HFN) with respect to their obese non treated littermates (HF), which was sustained after 22 days (Figure 1B; $P$ <0.05, Two-way ANOVA, Tukey post-test). At the end of the treatment, hepatic $NAD^+$ content was measured by HPLC, showing the expected oscillation with a peak at ~ZT12 in control mice (CD, Figure 1C) which is mostly disrupted in HFD fed mice (HF, Figure 1C, S1E)[16,21,36,46]. Importantly, in the HFN group, the acrophase of $NAD^+$ was restored to ZT12 (HFN, Figure 1C, S1E), hence daily rhythms in hepatic $NAD^+$ content was reinstated in obese mice (Figure S1D; $P$<0,001, $F$-test performed with CircWave).

We sought to assess physiological indicators of metabolic health and found that circulating insulin levels were much lower in the HFN group when compared to the HF group, with a major effect during the early active phase (Figure 1D, ZT12-18, $P$<0,001 Two-way ANOVA, Tukey post-test) and a six-hour phase delay in the oscillatory pattern (Figure S1F). Indeed, circulating insulin in HFN mice appeared largely comparable to their control littermates. Overall, we didn´t find major differences in body temperature between treated and untreated obese mice, suggesting that circadian-controlled thermogenic processes[48] are probably not involved in the metabolic benefits observed upon restoring $NAD^+$ oscillations (Figure S1 G-J).

It has been extensively demonstrated that glucose tolerance and insulin sensitivity follow daily rhythms imposed by the circadian system[49], hence we evaluated them at two different time points, ZT4 and ZT16. As expected, before $NAD^+$ treatment, HFD fed mice showed impaired glucose tolerance at both ZT (Figure S1K, S1L). Remarkably, after 10 days, restoring $NAD^+$ oscillations in obese mice significantly ameliorated glucose tolerance, specifically at ZT16 (Figure 1E, 1F, AUC HF vs HFN at day 10: $P$=0,0021, one-way ANOVA, Tukey post-test).

After 20 days of treatment, this improvement was also apparent at ZT4 (Figure 1E, AUC HF vs HFN at day 20: *P*<0,01, one-way ANOVA, Tukey post-test). As both insulin and glucose levels were lower in $NAD^+$ treated mice, insulin sensitization might occur. Accordingly, glucose clearance upon insulin IP injection was largely enhanced by $NAD^+$ chronotherapy (Figure 1G, 1H, S1M, S1N). Notably, this effect was already evident in the HFN group after 10 days of treatment independently of the time when measurements were performed (Figure 1G, 1H. AUC HF vs HFN at day 10: *P*<0,001, one-way ANOVA, Tukey post-test). Interestingly, $NAD^+$ treatment at ZT11 promoted a slight, albeit not significant, improvement in insulin tolerance respect to control lean mice when tested at ZT16 (Figure 1H). These results demonstrate that a chronotherapy with $NAD^+$ injected just before starting the active phase improves glucose tolerance by increasing insulin sensitivity in DIO mice. Collectively, the restitution of $NAD^+$ bioavailability at ZT12 recovers its basal hepatic oscillation and reverses the metabolic syndrome associated to diet-induced obesity.

Histological staining with Oil-Red-O (ORO) was used to semi-quantitatively assess hepatic steatosis (Figure 2A), revealing that obese mice treated with $NAD^+$ significantly decreased hepatic neutral lipid content (Figure 2B, 2C, One-way ANOVA, Tukey's posttest). Furthermore, a quantitative assay specific for hepatic triglycerides, the major form of fatty acids storage, revealed that these were globally reduced in obese mice after restoring hepatic $NAD^+$ oscillations (Figure 2D, Two-way ANOVA, Tukey's posttest). Importantly, the $NAD^+$ treatment recovered their oscillatory pattern which is generally disrupted in obese mice [16] (Figure 2D, S2). Additionally, this timed $NAD^+$ therapy reduced the accumulation of carbonylated proteins in liver lysates to normal levels (Figure 2E), and augmented mitochondrial biogenesis (Figure 2F). Together, these results indicated that increasing hepatic $NAD^+$ levels at ~ZT12 recovers

glucose homeostasis and successfully restrains liver pathology and oxidative stress of HFD-fed mice.

At the molecular level, the master regulator of lipid metabolism PPARγ protein[50] was overexpressed across the day in the livers from HFD-fed mice, while those treated with $NAD^+$ showed markedly reduced PPARγ levels (Figure 2G). A similar trend was evidenced for the transcription factor CEBPα, a known positive regulator of *Pparγ* gene expression and adipogenesis[51,52] (Figure 2G), further reinforcing the notion that a gene expression program involving lipid metabolism might be modified in $NAD^+$ treated mice.

**Extensive transcriptional reorganization driven by timed $NAD^+$ treatment.**

To address the extent of the transcriptional rewiring in the liver of $NAD^+$-treated obese mice, we performed a transcriptomic analysis at light (ZT6) and dark (ZT18) phases in mouse livers from CD, HF and HFN groups. 76 common genes were differentially expressed (DE) between day and night in all groups (Figure 3A, Table S1), with comparable expression levels. Amongst these, a number of transcripts related to circadian control were apparent, including *Clock*, *Arntl* (*Bmal1*), *Cry1*, *Nr1d2* (*Rev-Erb*β), *Rorc*, *Tef*, *Nfil3* or *Ciart* (Figure 3A, Table S1), suggesting that circadian rhythms were mostly preserved by the $NAD^+$ treatment at ZT11. Accordingly, rhythms in the core clock proteins BMAL1, CRY1, PER2 and REV-ERBα were overall sustained in the HFN group (Figure 3B, 3C). Interestingly, a significant reduction in CRY1 protein levels at ZT12 was observed in the HFN group compared to the HF (Figure 3B, 3C).

An extensive circadian transcriptional reprogramming is induced by high fat diet in the liver[16,53], hereafter we identified 524 day-to-night DE transcripts in CD mice, 1684 in HF mice and 599 in the HFN mice (Figure 3D, >1,25 fold-change, $P<0.05$). Out of these, 322 transcripts were

exclusively fluctuating in the CD group, 1327 fluctuated solely in the HF, interestingly, 306 newly fluctuating transcripts appeared in the HFN group (Figure 3D, 3E, Table S1). Functional analyses revealed that indeed, many of these DE genes participated in shared biological processes including transport, metabolic processes and response to oxygen (Figure 3F, Table S1). As expected, day-to-night transitions in gene expression were more evident for genes implicated in lipid metabolism in HFD-fed mice independently of $NAD^+$ treatment (Figure 3G, Table S1). Remarkably, a set of genes functionally related to immune system processes appeared significantly enriched solely in the HF mice (Figure 3G, Table S1). Interestingly, timed $NAD^+$ supply imposed new and specific day-to-night transcriptional fluctuations in genes functionally related to response to stress and starvation (Figure 3G, Table S1). Hence, we reasoned that a time-of-day specific transcriptional response to $NAD^+$ might be responsible for the beneficial effects of rhythmic restitution of this metabolite.

To further dissect the expression program imposed by $NAD^+$, we identified DE genes between groups, examined specifically at day (ZT6) or night (ZT18). At ZT6, 724 hepatic transcripts were significantly DE between CD and HF mice, while 936 transcripts varied when comparing HF and HFN groups, with 182 (12%) overlapping transcripts (Figure 4A, Table S2). At ZT18, 1731 genes were DE in livers from CD and HF mice, and 698 were DE between HF and HFN mice, appearing 118 (5%) common transcripts (Figure 4A, Table S2). Interestingly, most of these DE shared transcripts recovered their expression in the obese $NAD^+$ treated (HFN) mice to control conditions (Figure 4B). Common DE genes between CD-HF and HF-HFN comparisons at ZT6 were specifically enriched for biological processes related to regulation of the immune response, including both innate and adaptive immune system pathways (Figure 4C, Table S2). Furthermore, a direct assessment for distinctive gene sets between HF and

HFN groups at ZT6 using GSEA[54] (Gene Set Enrichment Analysis) showed that IL6-JAK-STAT3 and TGFβ signaling were the highest enriched hallmarks (Figure S3A). Indeed, timed $NAD^+$ treatment in obese mice suppressed the hepatic expression of inflammatory markers including *Stat3*, *Stat6*, *Tgfb1*, *Il1r1*, *Il6st*, *Tnfrsf1a*, *Tnfrsf1b, Smad3* or *Smad6* (Figure S3B). This supports the notion that timed $NAD^+$ treatment just before the onset of the active phase in obese mice abolishes the inflammatory environment associated with insulin resistance in NAFLD[55,56] specifically during their resting period. Accordingly, at ZT18, genes recovered to normal conditions by $NAD^+$ appeared mostly enriched for Lipid Metabolic Processes, particularly fatty acid biosynthesis and storage (*Plin2*, *Abhd5*, *Acsm1*, *Hsd17b12*, *Chka*) (Figure 4D, Table S2). Furthermore, a GSEA comparing HF and HFN groups at ZT18 revealed highest enrichment in the hallmarks Cholesterol Homeostasis and MTORC1 Signaling (Figure S3C), with significant downregulation of transcripts coding for major regulatory proteins and rate-limiting enzymes triggered by *de novo* $NAD^+$ oscillations (Figure S3D; Cholesterol Homeostasis: *Hmgcr*, *Hmgcs1*, *Sqle*, *Acss2*, *Lss* or *Stard4*; MTORC1 signaling: *Acaca*, *Acly*, *Me1*, *Adipor2*, *Psma3*, *Psma4*, *Psmd14* or *Psmc6*). As shown, these hepatic expression changes at ZT18 were accompanied by improvement of hyperlipidemia and fatty liver traits after restoring $NAD^+$ oscillations in obese mice (Figure 2A-D). Pathway analyses revealed transcriptional mechanisms restituted by $NAD^+$, with significant enrichment of NFkB, HIF1 and HNF3 transcriptional networks (Figure 4D); and *de novo* motif discovery in the promoters of genes whose expression appeared dysregulated only in the HF group identified strong similarities to NFkB-p65/RELA and FOXA1/FOXA2 (HNFα/HNF3β) binding sites (Figure 4E). Accordingly, out of 83 transcripts recovered by $NAD^+$ at ZT18, 11 (13%) are previously described direct targets of FOXA2[57] (Figure S3E); interestingly, FOXA2 is a key regulator of

lipid metabolism which becomes dysregulated in diabetic, insulin resistant mice[57,58]. Together, these data indicate that the inflammatory transcriptional signature related to NAFLD is abolished after timed $NAD^+$ treatment, possibly through coordinating the action of transcription factors such as NFkB or FOXA2, and intracellular signaling involving the MTORC1 pathway.

**Insulin signaling and rhythmicity in nutrient sensing pathways are rescued by $NAD^+$ oscillations in obese mice.**

Transcriptional networks uncovered in these analyses together with measurements of metabolic parameters are strongly suggestive of restored insulin sensitivity and nutrient sensing molecular pathways after reestablishing $NAD^+$ oscillations in obese mice. To confirm this at the molecular level, we first evaluated phosphorylation of AKT1, a key kinase effector of insulin signaling[59], along the day. As previously described, AKT1 phosphorylation at Ser 474 (p-AKT(S473)) appeared cyclic in CD fed mice[60], with a peak at ZT18 (Figure 4F, S4A), coincident with highest food intake (Figure S1C). In contrast, in HFD fed mice, p-AKT(S473) was constitutively low, suggestive of insulin resistance in the liver of obese mice (Figure 4F, S4A). Remarkably, we found restoring hepatic $NAD^+$ oscillations in obese mice specifically increased p-AKT(S473) at ZT12 (Figure 4F, S4A. $P$<0,0001; two-way ANOVA, Tukey post-test), hence imposing daily oscillations to insulin signaling. Furthermore, diurnal rhythms in AMPK phosphorylation at T172 were also restored by $NAD^+$ treatment in obese mice, although with a unique peak at ZT12, which was six hours phase delayed compared to their control, lean littermates (Figure 4F, S4B). This is in keeping with our previous observation of a reduction of CRY1 protein in the HFN group specifically at ZT12 (Figure 3B, 3C), as AMPK rhythmically phosphorylates and destabilizes CRY1[61]. Concomitantly, the AMPK substrate ULK[62] appeared hyperphosphorylated in the livers of $NAD^+$ treated mice at ZT12 (Figure S4C).

Following the lead from our transcriptomic analyses, we also explored mTORC1 function. mTOR S2448 phosphorylation and activity appear rhythmic in the mouse liver, coordinating a number of functions around the day, including ribosome biogenesis[63,64] (Figure 4G). High fat feeding constitutively induced mTOR phosphorylation, and timed $NAD^+$ treatment in obese mice downregulated it (Figure 4G, S4D). We investigated the phosphorylation of p70-S6K (S6K) as a readout of the activity of mTORC1[65], and found that the diurnal profile of activation of S6K-Thr389 phosphorylation was completely restored by $NAD^+$ chronotherapy in the livers of HFD-fed mice (Figure 4G, S4E). Additional mTOR downstream signaling revealed by phosphorylation of 4EBP1(Thr37/46) was reduced in obese, $NAD^+$ treated mice (Figure 4G, S4F). We also observed that the mTORC1 agonist p90-S6K (RSK)[65,66] and its activity as monitored by its phosphorylation in the Thr359 were significantly downregulated in the HFN group respect to the HF (Figure 4G, S4G). These results reinforce our pathway and gene set enrichment analyses comparing HF and HFN groups, consistent with reduced function of mTORC1 pathway after recovering $NAD^+$ oscillations in obese mice.

**A unique $NAD^+$ transcriptional signature identifies new pathways linked to metabolic improvement.**

We sought to explore the transcriptional signature induced by oscillatory $NAD^+$, by identifying DE genes specifically in the HFN group. We found just 74 genes changing their expression at ZT6, and 196 at ZT18 (Figure 4H, 4I, Table S3). Functional analyses did not retrieve any significant enrichment for these genes at ZT6; however, it became very evident that at ZT18, a large part of the DE genes after $NAD^+$ treatment were overexpressed and functionally involved in intracellular vesicle transport and catabolic processes (Figure 4I, 4J, Table S3). Indeed, five members of the Rab family of small GTPases, know regulators of membrane trafficking[67], were

specifically overexpressed after $NAD^+$ treatment, including *Rab1b*, *Rab7a*, *Rab10* which are largely involved in mediating autophagy[68-71], and *Rab6a*, *Rab8a*, which also mediate receptor trafficking in response to insulin signaling[72,73]. Additional overexpressed genes by $NAD^+$ known to regulate autophagy were *Psen1*[74], *Vps28*[75].

A search for *de novo* motif enrichment within the promoters of $NAD^+$-induced genes yielded matrices with high similarity to the binding sites for NR2E1 (TLX) and HNF4$\alpha$ TFs, both implicated in maintaining lipid homeostasis in the liver [76,77]. Also, a motif recognized by IRF3 and NR4A1 (Nur77) appeared significantly enriched (P= 1e-5), and interestingly, Nur77 has been shown to regulate the cytoplasmic shuttling of LKB1, hereby phosphorylating and activating AMPK[78]. Together, these data indicate that oscillatory $NAD^+$ in obese mice activates a gene expression program favoring processes highly demandant for vesicle trafficking, such as translocation of membrane receptors or autophagy, and reinforce the idea of pharmacological supply of $NAD^+$ preferably targeting activation of AMPK even in the context of high caloric feeding.

**Time-of-day determines the efficacy of $NAD^+$ as a treatment for diet-induced metabolic dysfunction.**

To investigate if the beneficial effects of pharmacological restitution of $NAD^+$ oscillations depend on the time of the day, we supplied $NAD^+$ in opposite phase to its natural rhythmicity, hereby at the end of the active phase in mice, ZT23 (HFN23 group). In these HFN23 mice, oscillations of hepatic $NAD^+$ were induced with antiphase respect to CD and HFN mice, showing a peak at ZT0 and decreasing at ZT12-18 (Figure S5A, S5B). As shown in mice treated at ZT11 (HFN), these also showed mild, albeit non-significant, weight loss after one week of treatment (Figure 5A, week 9). Contrary to the HFN group, mice supplied at ZT23

gained weight during weeks 10 and 11 (Figure 5A). Instead, after three weeks of treatment, mice treated with $NAD^+$ at ZT11 had lost ~5% of body weight, while those treated at ZT23 were ~2% heavier (Figure 5B), illustrating significant differences on the efficacy of the treatment depending on the time of administration. Notably, total food intake was comparable for all high-fat fed mice, and before and after the treatment no significant differences were found (Figure 5C, S5C, Two-way ANOVA with post-test). Serum insulin was significantly higher in mice injected at ZT23 particularly during the dark phase (Figure 5D, S5D), indicating insulin resistance in these mice, although $NAD^+$ therapy was effective to reduce fasting serum glucose independently of the time of supply (Figure S5E). These results indicate that in obese mice treated with $NAD^+$ at ZT23, insulin clearance or the feedback inhibition of insulin secretion are impaired, which is a sign of persistent metabolic dysfunction in these mice[79]. Along these lines, we performed GTT and ITT at ZT4, because the effects of $NAD^+$ supply at ZT11 tended to be more pronounced during the light phase (Figures 1E-H). We found that at the end of the treatment with $NAD^+$ at ZT23 (day 20, HFN23), glucose and insulin tolerance showed non-significant improvement compared to the HF-fed mice. Actually, the $NAD^+$ treatment at ZT11 was significantly more favorable to improve glucose homeostasis than at ZT23 (Figures 5E, 5F, S5F, S5G; One-way ANOVA followed by Tukey's posttest). Quantification of the relative improvement to the obese non-treated mice showed that after 10 days of treatment, $NAD^+$ was effective to improve GTT and ITT only when supplied at ZT11, but not at ZT23. At the end of the treatment (day 20), $NAD^+$ supply at ZT11 showed still significantly better performance than at ZT23 (Figure 5G, Two-way ANOVA followed by Tukey's posttest).

Circulating triglycerides, largely known to be reduced by the $NAD^+$ precursor niacin[80,81], were decreased along the day to normal levels by $NAD^+$ only when the treatment was performed at ZT11, but not at ZT23 (Figure 5H). Interestingly, serum triglycerides were rhythmic for all groups; yet specific to the HFN23 group was that highest levels appeared at daytime, thus presenting antiphase daily oscillations (Figure 5H). We found a very significant reduction in serum triglycerides only when $NAD^+$ was injected at ZT11, while injection at ZT23 kept serum triglyceride levels significantly higher than injection at ZT11 (Figure 5H, $P$<0,05; One-way ANOVA with Tukey's post-test). Besides, hepatic steatosis was reduced to a similar extent in HFN and HFN23 groups (Figure 5I-K, S5G-I). However, we observed opposite daily dynamics in hepatic PPAR$\gamma$ protein levels, and in its transcriptional activator CEBP$\alpha$ (Figure 5L-M), which together with the serum triglycerides analyses, suggest that lipid metabolism might be distinct.

**$NAD^+$ chronotherapy at ZT11 effectively coordinates hepatic intracellular signaling and gene expression driving lipid oxidation.**

To further disentangle the molecular pathways responsible for the physiological differences in glucose and insulin tolerance, and circulating triglycerides, between HFN and HFN23 groups of obese mice, we compared nutrient sensing signaling in the liver from these mice. Western blot experiments showed that providing $NAD^+$ at ZT23 to obese mice did not recapitulate hepatic AKT phosphorylation and activity, as did at ZT11 (Figure 6A-B), hereby confirming that insulin signaling remains defective in mice treated at ZT23, as suggested by the ITT (Figure 5F, S5B). Additionally, the response to starvation signaling converging into AMPK-T172 phosphorylation and subsequent activation triggered at ZT12 after reinstating $NAD^+$ oscillations was not induced in the livers of the HFN23 group (Figure 6A-B). Furthermore,

nutrient sensing by mTOR pathway appeared active through the day in livers from HFN23 group, as shown by persistent phosphorylation of p70-S6K-T389 (Figure 6C-D), and contrasting with the rhythmic pattern observed in the HFN11 group. Moreover, RSK-T359 appeared hyperphosphorylated in the HFN23 group, also showing antiphase dynamics compared with the HFN group (Figure 6C-D). These data clearly show that increased $NAD^+$ levels at the end of the activity period are less efficient in synchronizing mTOR signaling pathway than high $NAD^+$ at the onset of activity, and reinforce the notion of a chronotherapeutic approach as the best therapy for the treatment of metabolic diseases by $NAD^+$ boosters.

It is widely accepted that AMPK regulates lipid metabolism through phosphorylation of acetyl-CoA carboxylase 1 (ACC1) at Ser79 and ACC2 at Ser212. These in turn downregulate the production of malonyl-CoA, the major substrate for fatty acid synthase (FAS) and a strong inhibitor of carnitine palmitoyl transferase 1 (CPT1). Consequently, fatty acid synthesis is suppressed in favor of lipid oxidation, partially through activation of the rate limiting step sustained by CPT1[82]. Additionally, increased fatty acid oxidation has been largely recognized as a major metabolic outcome after pharmacological increase of $NAD^+$ [40,83], and this process appears rhythmic in mouse liver with increased rate near the end of the rest period [21]. Also, our gene expression data revealed a unique $NAD^+$ transcriptional signature involving genes pertaining to catabolic processes at ZT18 (Figure 4J). Hence, we sought to explore the diurnal transcriptional profile of genes involved in lipid oxidation. Selected transcripts from the microarray data and the key rate-limiting enzymes *Cpt1a*, *Cpt2*, *Acox1*, *Abcd1* were quantified in the livers from all groups (Figure 6E-G). As expected, we found that genes involved in β-oxidation, either mitochondrial (*Cpt1a*, *Cpt2*, *Acot2*, *Crat*, *Acaa1b*, *Acsm1*, *Echs1;* Figure 6E)

or peroxisomal (*Acox1*, *Abcd1*, *Slc27a2;* Figure 6F), and in ω-oxidation (*Cyp4a10*, *Cyp4a14*, *Cyp4a31;* Figure 6G) were globally overexpressed in HFD-fed mice compared to lean mice[84]. Interestingly, almost all genes were significantly overexpressed specifically at ZT18 in obese mice treated with $NAD^+$ at ZT11 (HFN), but not at ZT23 (HFN23). Indeed, fatty acid oxidation-related genes were highly expressed at the end of the rest period (~ZT12)[84]; yet, unique to the HFN group was that the breadth of transcriptional activity further extended through the active period, reaching significantly higher levels than in the non-treated, obese mice (HF) at ZT18 (Figures 6E-G, *P*<*0,05, **0,01, ***0,001 Two-way ANOVA with Tukey post-test). Hereby, expression of these genes at ZT18 was altered depending on the time of $NAD^+$ treatment, in a way that the treatment at ZT11 significantly enhanced their expression, whereas in mice treated at ZT23, expression was significantly reduced to levels largely comparable to the CD littermates (Figure S6C, One way ANOVA with Tukey posttest). Accordingly, housekeeping genes *Tbp* and *Rplp* presented no significant variations (Figure S6D). Together, these data suggest that increased hepatic $NAD^+$ levels at the beginning of the active phase induce AMPK-phosphorylation and activity, favoring a transcriptional program of genes involved in fatty acid oxidation which extends through the active phase, possibly contributing to weight loss and decreased hepatic and circulating triglycerides specifically in HFN mice.

While obese mice treated with $NAD^+$ at ZT23 presented some metabolic ameliorations mostly consisting of improved glycemic levels and reduced hepatic steatosis, we did not find consistent changes in gene expression or nutrient sensing signaling. Intriguingly, our microarray data showed that transcripts with highest fold change after $NAD^+$ treatment were Metallothionein 1 and 2 (*Mt1* and *Mt2*), two antioxidants and longevity regulators known to protect from HFD-induced obesity[85-87], and these transcripts were significantly more

overexpressed in obese mice treated with $NAD^+$ at ZT23 (Figure S6E, P<0,001 HFN vs HFN23; Two Way ANOVA with Tukey´s posttest). A similar case was found for the gene lipocalin 2 (*Lcn2*), which encodes for a secreted protein protective against NAFLD[88]. Hence, while $NAD^+$ chronotherapy works optimally at ZT11, its supply at ZT23 induces distinct protective pathways responsible for a mild, albeit noticeable, improvement of HFD-induced metabolic disease.

**Timed $NAD^+$ treatment resets the hepatic clock.**

Chronotherapy with $NAD^+$ at ZT11 and ZT23 led to significantly different consequences in metabolic fitness and daily gene expression in the liver of obese mice. Hence, we reasoned that the molecular clock might be responsible for daily variations in the effectiveness of the treatment. Thereby, we compared the hepatic clock protein expression along the day between obese mice treated at ZT11 and at ZT23 (Figure 7A). Western blot analyses revealed a remarkable impact of $NAD^+$ treatment at ZT23 in the dynamic expression of the clock proteins CRY1, PER2 and REV-ERB$\alpha$, which displayed an almost complete antiphase dynamic (Figure 7A, 7B). Concomitantly, BMAL1 phosphorylation was also 6-10 hours phase-shifted by $NAD^+$ treatment at ZT23, being higher at ZT0 (Figure 7A, 7B, Two-Way ANOVA). Subsequently, we explored the expression of clock genes across the day (Figure 7C). Strikingly, $NAD^+$ treatment at ZT23 in obese mice induced a transcriptional rewiring of clock genes, whose expression almost perfectly mirrored that of the other groups, demonstrating that at ZT23, $NAD^+$ synchronizes the hepatic clock genes' expression. Consequently, the average acrophases of the oscillations, defined as the highest point of the fitted wave by CircWave, was phase shifted by 10-12 hours in the HFN23 group in all tested clock genes, both activators (*Bmal1*, *Clock*) and repressors (*Cry1*, *Per1*, *Per2* and *Rev-Erb*$\alpha$) (Figure 7C, S7E). Indeed, $NAD^+$

chronotherapy did not compromise rhythmicity in clock gene expression (Figure S7E, $P$<0,05; CircWave $F$-test). To determine whether the observed antiphase dynamic of the clock transcriptional regulators was functional, we selected the genes *Dbp*, *Tef*, *Nfil3* and *Noct*, whose expression is directly and mostly controlled by the core clock machinery, and analyzed their hepatic expression around the day (Figure 7D). Coincident with the clock gene expression, the daily transcriptional profile of clock-controlled genes appeared rhythmic for all groups, and phase-inverted specifically in the obese mice treated with $NAD^+$ at ZT23, with a significant phase shift of 11-13 hours for *Dbp*, *Tef* and *Noct*, and ~8 hours for *Nfil3* expression (Figure 7D, S7E). Because redox rhythms regulate DNA binding of CLOCK:BMAL1 heterodimers *in vitro*[89], and the $NAD^+$ precursor NR increases BMAL1 recruitment to chromatin in livers from aged mice[46], we hypothesized that inverted expression of clock genes in HFN23 might be driven by time-specific recruitment of BMAL1 to chromatin. To test this, we performed ChIP analyses to measure BMAL1 binding to regulatory E-boxes of clock and clock-controlled genes (Figures 7E and 7F). As described[90], we observed increased recruitment of BMAL1 at ZT6 in livers from CD, HF and HFN groups of mice for all tested E-boxes. Notably, in livers from HFN23 mice, BMAL1 binding appeared significantly increased at ZT18, consistent with inverted expression (Figures 7E, 7F; $P$<0.05, Two-way ANOVA with Tukey´s post-test). A non-related region at the 3' UTR region of *Dbp* gene was used as a negative control. We further evaluated the effect of $NAD^+$ supplementation in the expression of $NAD^+$ biosynthesis and salvage genes *Nmrk1*, *Nampt*, *Nmnat3* and *Nadk* which also showed inverted phase specifically in HFN23 mice (Figure 7G). Accordingly, BMAL1 binding to their regulatory elements was increased at ZT18 in HFN23 mice, yet specific to these group of genes was that $NAD^+$ treatment significantly potentiated BMAL1 recruitment to chromatin. Finally, we explored

the expression from TFs collaborating with the clock machinery to sustain a rhythmic transcriptional reprogramming in obesity[16,84]: *Pparg2*, *Ppara* and *Srebf1c.* Transcription for these genes was phase-inverted specifically in HFN23 mice, which was also accompanied by differential BMAL1 chromatin recruitment (Figure 7H). Also, expression levels of additional TFs related to hepatic lipid metabolism *Hnf4a*, *Foxa2*, *Foxo1* and *Cebpa* were altered to a similar extent (Figure S7B). Antiphase expression of key transcription factors regulating hepatic lipid metabolism might underlie the inverted pattern of circulating triglycerides in HFN23 mice (Figure 5H), but other lipids synthetized in the liver might be affected. Accordingly, hepatic cholesterol levels also showed a phase inverted pattern in the liver of HFN23 mice (Figure S7C, S7D), reinforcing the idea that $NAD^+$-mediated synchronization of transcriptional rhythms in the liver inverts hepatic lipid metabolism. Together, this data demonstrates a time-dependent transcriptional response to $NAD^+$ therapy in the liver of obese mice, through the synchronization of BMAL1 recruitment to chromatin and rhythmic transcription of clock and clock-controlled genes. Hereby, BMAL1 plays a pivotal role translating fluctuations in $NAD^+$ levels to shape circadian transcription.

A phase-inverted hepatic clock has been previously shown for mice subjected to inverted feeding rhythms, where the SCN clock remains aligned to light-dark cycles[91,92]. At this regard, in all tested groups of mice, clock gene expression in the SCN remained largely intact after $NAD^+$ treatment (Figure 8A, Two-way ANOVA), and locomotor behavior analyses showed that overall, $NAD^+$ treatment preserved alignment between light-dark and rest-activity patterns (Figure 8B). Quantification of locomotion in 30 minutes bins revealed that after $NAD^+$ treatment, mice became significatively less active for either 90 minutes (HFN) or 30 minutes (HFN_23) windows (Figures 8C, S7E, Two-way ANOVA followed by Sidak's posttest). We next

questioned whether feeding cycles might be altered by $NAD^+$ treatment because as previously reported, this is a cause for uncoupled central and peripheral clocks[91,92], while $NAD^+$ itself can influence feeding behavior through implicated hypothalamic circuits[93,94]. Notably, daily food intake appeared rhythmic and aligned to light-dark cycles for all groups of HF diet fed mice (Figures 8D, 8E), showing a more robust day-to-night difference the obese mice treated with $NAD^+$ at ZT11 (Figure 8E). Furthermore, we found similar observations when applying a therapy with the $NAD^+$ precursor nicotinamide (NAM), which was previously described to boost hepatic $NAD^+$ after IP injection in one hour[95]. Hence, three weeks with NAM chronotherapy performed best when applied at ZT11 to improve body weight, GTT and ITT (Figure S8A-D, Unpaired Student´s *t* test). As shown for $NAD^+$, the NAM treatment at ZT23 inverted the expression of the hepatic molecular clock (Figure S8E), while keeping behavioral locomotor activity in phase with light/dark cycles (Figure S8F). This reinforces the notion that $NAD^+$ can potentially synchronize the hepatic molecular clock, by resetting clock gene expression to adjust its phase to the time of the day when $NAD^+$ bioavailability is higher. Collectively, these data support that boosting $NAD^+$ levels is an effective treatment for HFD-induced metabolic disease, and demonstrate that a chronotherapeutic approach is significantly more beneficial when $NAD^+$ increases at the onset of the active phase.

## DISCUSSION

In the past decade, therapies oriented to increase endogenous $NAD^+$ levels have received much attention as treatments for metabolic disorders. Mounting research in rodents demonstrate that pharmacological approaches using “$NAD^+$ boosters” treat the physiopathology of diet and age-associated diabetes in mice, and reverse cardiovascular

493 disease or muscle degeneration[83]. In humans, the $NAD^+$ precursor niacin has been largely
494 used to treat dyslipidemia, and a number of clinical trials are ongoing for other $NAD^+$
495 precursors[96]. However, all these studies and clinical protocols mostly disregard the reciprocal
496 interactions between circadian rhythms and $NAD^+$ metabolism. Here, we demonstrate that
497 $NAD^+$ can shift the phase of the hepatic molecular clock while preserving the SCN clock largely
498 intact, and concomitantly, the efficacy of increasing $NAD^+$ levels to correct metabolic diseases
499 depends on the time-of-day (Figure 8F).

500 $NAD^+$ and its phosphorylated and reduced forms, $NADP^+$, NADH and NADPH, are
501 fundamental compounds in intermediary metabolism as hydride-accepting or -donating
502 coenzymes in redox reactions[97]. $NAD^+$ is produced in all tissues from the salvageable
503 precursors NAM, nicotinamide riboside (NR) or niacin, while some tissues such a liver produce
504 $NAD^+$ *de novo* from tryptophan, in a much less efficient biosynthetic pathway [30,98]. It is
505 generally accepted that NR or NAM enter the cell[99], while extracellular $NAD^+$ and NMN are
506 converted to NR[100]. At this regard, the $NAD^+$ precursors NAM, NMN and NR have been
507 preferentially used as $NAD^+$ boosters; however, we set up a therapy with $NAD^+$ because the
508 limited data tracing metabolic fluxes suggest distinct, tissue-specific effects of NR and NMN[101].
509 Moreover, $NAD^+$ uptake appears fast and effective in cells, and a mitochondrial active
510 transporter has been recently described[102-105]. Yet, to gain insights into the bioavailability of
511 $NAD^+$ precursors in our study, it would be necessary to unravel the hepatic $NAD^+$ metabolome
512 in all tested conditions, as for example, the possibility that time-dependent decline in NADPH
513 and $NADP^+$ levels in livers from obese mice[27,35,106] contributes to differences between HFN
514 and HFN23 mice cannot be ruled out, constituting a limitation of our study. However, we
515 demonstrated that hepatic $NAD^+$ levels raised within an hour after IP injection in obese mice,

and followed a circadian turnover when administered at ZT11, at the onset of the active phase (Figure 1B). This chronotherapy recapitulated the metabolic improvements to a similar extent to the previously reported for the $NAD^+$ precursors NMN[36,107,108] and NR[32,35,40,43,44,109-111], mostly consisting of decreased weight gain, improved insulin sensitivity and glucose tolerance, decreased circulating leptin and triglycerides, and amelioration of NAFLD with decreased hepatic pro-inflammatory transcriptional signature (Figures 1, 2, 3). At the molecular level, we demonstrated that, upon $NAD^+$ chronotherapy, daily rhythms were restored for hepatic insulin and nutrient signaling. This was evidenced by rhythms in AMPK-T172 and AKT-S473 phosphorylation, and mTORC1-directed pS6K phosphorylation, which became oscillatory with peaks during the active phase (ZT12-18; Figure 4F, 4G). Accordingly, we also observed decreased phosphorylation of p90RSK-T359 (Figure 4G), a positive effector of mTORC1 signaling and driver of NFκB activity[112,113]. It appears conflicting that the AMPK response to starvation and the mTORC1 nutrient sensing pathways became active at concurrent times during the day after restoring $NAD^+$ oscillations in obese mice, as they usually signal opposed nutritional states and engage into regulatory negative feedback loops[114]. However, recent research shows that specific activation of AMPK exists which does not lead to mTORC1 inhibition, but instead sustains ULK1 activity and autophagy to preserve protein homeostasis[115], which is in keeping with our findings (Figure 4F, 4G, S4C). Notably, a hepatic $NAD^+$-specific transcriptional signature emerged in treated mice related to intracellular trafficking, consisting of overexpression of the Rab GTPase network regulator of autophagy[70], further reinforcing the notion that $NAD^+$ preferably targets AMPK signaling to activate autophagy and possibly, translocation of membrane receptors. Along these lines, AMPK has

been largely recognized as a therapeutic target for metabolic diseases[116,117], yet the well-known circadian fluctuations in its activity[118] have been fully overlooked for treatment.

We have demonstrated a time-of-day dependent response to $NAD^+$ therapy. We observed significant differences between obese mice treated at ZT11 or at ZT23, where the latter did not completely recapitulate the metabolic improvements generally resulting from analogous therapies. Concomitantly, $NAD^+$ therapy at ZT23 did not trigger AMPK phosphorylation neither rewiring of mTORC1 signaling in the liver of obese mice. Strikingly, the expression dynamics of the molecular clock were completely phase inverted in livers from HFN23 and HFNAM_23 mice, showing that at the onset of the active phase, $NAD^+$ can efficiently reset the phase of the hepatic clock (Figures 7, 8, S8). These findings support earlier evidence that specific nutritional cues are potent zeitgebers for peripheral oscillators[16,47,91,119], and reinforce the existing notion of autonomous regulation of hepatic $NAD^+$ metabolism closely linked to the clock function[26]. Together with our findings, this suggests that the molecular clock acts as a key interface to induce timing-specific modulation of nutrient and insulin signaling by $NAD^+$.

Our analyses revealed substantial differences in expression from genes involved in fatty acid oxidation, with marked downregulation in obese mice treated with $NAD^+$ at ZT23 (Figure 6E-G, S6C). In mouse liver, these genes are oscillatory with a peak of expression at the end of the rest phase[84]. Their expression is to some extent clock-controlled; however, their transcriptional regulation mostly relies on nutritional cues integrated by intracellular signaling, multiple nuclear receptors and transcription factors such as PPAR$\gamma$, PPAR$\alpha$ or SREBP1, epigenetic regulators including MLL1 or SIRT1, and even neural circuits[16,84,120-122]. Untimed $NAD^+$ rise, through resetting the circadian machinery and the subsequent misalignment from feeding rhythms, might hinder the coordinated action between the clock and cooperative transcriptional

561 regulators on chromatin, hereby obstructing the adequate control of specific transcriptional
562 programs. At this regard, BMAL1 recruitment to chromatin was adjusted by timed $NAD^+$
563 treatment, and when administered at ZT23 leaded to phase-inverted transcription of direct
564 CLOCK:BMAL1 targets, as expected for a pioneer-like transcription factor[123,124]. In this
565 scenario, we found that several master regulators of rhythmic hepatic lipid and cholesterol
566 metabolism including *Pparα*, *Pparγ*, *Srebp1c*, *Cebpa*, or *Hnf4a*[16,84,125,126] were subjected to this
567 mechanism, and their phase inversion in HFN23 mice was accompanied by inverted rhythms
568 in hepatic cholesterol and circulating triglycerides. These results demonstrate that $NAD^+$
569 modulates BMAL1 recruitment to chromatin and shapes rhythmic transcription and
570 metabolism.

571 $NAD^+$ is a coenzyme in redox reactions, but also serves as a substrate of $NAD^+$ consuming
572 enzymes which cleave $NAD^+$ to produce NAM and an ADP-ribosyl product, such as ADP-
573 ribose transferases, cADP-ribose synthases and sirtuins (SIRT1-SIRT7)[97,127]. Indeed, both
574 $NAD^+$ consumers SIRT1[46,128,129] and SIRT3[21] provide reciprocal regulation to the clock
575 machinery to modulate circadian transcription and metabolism in the liver. Furthermore, recent
576 research shows that a $NAD^+$-SIRT1 interplay mediates deacetylation and nuclear translocation
577 of PER2 and, in line with our results, shapes BMAL1 function, while this control is altered in
578 livers from aged mice[46]. Through activation of SIRT1 and SIRT3, it is also possible that rising
579 $NAD^+$ at ~ZT12 might contribute to rhythmic lipid oxidation and mitochondrial function driven by
580 protein acetylation, including PPARγ [27,130], while keeping the hepatic clock aligned to the
581 external time. Yet, the regulation of the circadian system by sirtuins in health and disease
582 remains to be fully disentangled. Circadian misalignment imposed by antiphase $NAD^+$ in our
583 HFN23 and HFNAM_23 mice might obstruct metabolic improvements, through uncoupling of

584 the central light-synchronized and peripheral NAD⁺-synchronized clocks. Although hepatic
585 neutral lipid content was reduced independently of time-of-treatment (Figure 5I-K), significant
586 improvement of glucose homeostasis and hepatic insulin signaling were apparent only in HFN
587 mice. Indeed, circadian misalignment has been extensively reported to drive metabolic
588 dysfunction both in mouse and humans[131-133]. In this scenario, expression of clock genes in the
589 SCN was largely intact upon NAD⁺ injection, and consequently, locomotor activity remains
590 aligned with the light-dark cycles also in HFN23 mice (Figure 8A-C). Uncoupled liver and SCN
591 clocks have been previously reported in mice when access to food is restricted to the light
592 period[91,134,135]; however, our HFN23 mice did not show significant variations in eating behavior
593 (Figure 8D-E), evidencing that uncoupling the central and hepatic clocks is a time-dependent
594 effect of NAD⁺ supply. Notably, abnormal metabolic signaling triggered by high-fat diets
595 uncouples body clocks[15]; thus, it would be interesting to define which extra-hepatic oscillators
596 are reset by NAD⁺. At this regard, recent reports suggest that the brain blood barrier might be
597 permeable to NAD⁺ [136,137] in which case hypothalamic neurons could be influenced. Yet,
598 further research is necessary to decipher the extent of the modulation of brain clocks by
599 increased circulating NAD⁺ precursors. Additionally, our study is limited by the cellular
600 heterogeneity in fatty liver, with for example, infiltration of pro-inflammatory macrophages
601 which have been recently shown to limit NAD⁺ bioavailability through high expression of the
602 NAD-consuming enzyme CD38[138,139]. Hence, it is possible that time-dependent cellular
603 heterogeneity in liver[140] could contribute to the NAD⁺-dependent improvement of the metabolic
604 phenotype.

605 In humans, clinical trials aiming to boost endogenous NAD⁺ for treatment of metabolic
606 diseases are increasing, in many cases reporting conflicting results[127]. All these studies mostly

607 overlook the time of drug intake, which is selected based on practicalities or attempting to
608 displace side effects from the patient's active phase. Considering our results, we propose that
609 time of treatment dictates the amplitude of metabolic benefits from rising $NAD^+$ levels, which
610 ideally outlines the basic strategy of chronobiology-based $NAD^+$ therapy.

611

612 **METHODS:**

613 **Animals and diets**

614 Four-week-old male C57Bl/6J mice were obtained from the Biological Models Unit at the
615 Instituto de Investigaciones Biomédicas (UNAM, Mexico). The mice were kept under a 12:12-h
616 light:dark cycles. Food and water were provided *ad libitum*. Temperature and humidity were
617 constantly monitored. Mice were randomly distributed to three groups (20 mice/group). The
618 control group was fed during eleven weeks with normal chow (CD, 2018S Teklad, ENVIGO),
619 bearing 24% calories from protein, 18% calories from fat and 58% calories from
620 carbohydrates. The other two experimental groups were fed a high fat diet (HFD, based on
621 TD.160547 Teklad, ENVIGO), consisting of 15% calories from protein, 53% calories from fat
622 and 38% calories from carbohydrates, and customized to match $NAD^+$ dietary sources content
623 to that of the CD (0,2% tryptophan and 115 mg/kg nicotinic acid). Food intake and body weight
624 were measured once a week. For daily food intake measurements, mice were single housed,
625 and measurements were recorded for one week.

626 All animal experimental procedures were reviewed and approved by the Internal Committee for
627 the Care and Use of Laboratory Animals (CICUAL) at the Instituto de Investigaciones
628 Biomédicas, (UNAM, Mexico), and are registered under protocol no. ID240.

629

## Chronotherapy with $NAD^+$ and NAM

$NAD^+$ and NAM were purchased from SIGMA (cat. no. N7004, N0636) and were dissolved in 0.9% NaCl isotonic saline solution and filter sterilized. To determine the $NAD^+$ dose, we wanted to keep two premises: 1) to keep $NAD^+$ levels into the physiological range, and 2) avoid undesirable secondary effects of high doses. To do so, we chose the range of tested doses based on previous reports[94,141,142], and treated mice with IP injection of 800, 100, 50 or 10 mg/kg body weight, while keeping a constant volume of approximately 180 μl. Control mice were injected with isotonic saline solution. C57Bl/6J male mice (n=3) were IP injected, and sacrificed one hour later. $NAD^+$ was measured by HPLC as described below. Because we planned on a chronic treatment, the minimum dose inducing a statistically significant increase in hepatic $NAD^+$ with respect to control livers was selected as the experimental dose (Figure S1A, 50 mg/Kg of body weight: $P$ <0.001, One-way ANOVA with Tukey's posttest). Hence, for all experiments, mice were IP injected with 50 mg/kg of $NAD^+$ for 20 consecutive days, either at ZT11 (one hour before lights off), or at ZT23 (one hour before lights on). Of note, we didn´t find differences in hepatic $NAD^+$ at a dose of 10 mg/kg, a reason why we did not try lower concentrations. The dose for NAM treatment (200 mg/kg) was selected based on previous reports[95,143-145].

## Detection and quantification of $NAD^+$ by HPLC.

$NAD^+$ measurements were performed according to Yoshino and Imai 2013 [146], with subtle modifications. 100 mg of frozen tissue were processed in a final volume of 2 ml of 10% $HClO_4$ with a Polytron homogenizer (Kinematica CH-6010 Kiriens-Lu) and centrifuged at 13,000 rpm for 5 min at 4°C. The supernatant was neutralized adding a one-third volume of 3M $K_2CO_3$, and vortexed. After 10 min of incubation on ice, samples were cleared by a 13,000 rpm

centrifugation at 4ºC during 5 min. The supernatant was diluted at 30% with 50 mM phosphate buffer (3.85% of 0.5 M $KH_2PO_4$, 6.15% of 0.5 M $K_2HPO_4$, 90% HPLC grade water -v/v/v-, pH 7.0, filtered through a 0.22 µm filter and degassed). 50 µl of the samples were analyzed using a 1260 infinity quaternary LC VL HPLC system (Agilent) attached to a diode array detector. Analytes were separated on a ZORBAX Eclipse XDB-C18 4.6x150 mm, 5 µm column (Agilent p/n 993967-902). For the HPLC, the gradient mobile phase was delivered at a flow rate of 1ml/min, and consisted of two solvents: (A) 50 mM phosphate buffer pH 6.8 and (B) methanol 100%. The initial concentration of A was 100%, the solution was held into the column for 5 min and then B was progressively increased to 5% over 1 min, held at 5% B for 5 min, followed by an increase to 15% B over 2 min, held at 15% B for 10 min and returned to starting conditions of 100% A in 1min, and held at 100% A for 6 min. $NAD^+$ was detected using a sample wavelength of 261 nm and reference wavelength of 360 nm. Adequate standards including $NAD^+$ were used for calibration and identification of the retention/migration time of $NAD^+$ within the samples. Instrument control, data acquisition and analysis were performed using the Agilent ChemStation system for LC, according to manufacturer´s instructions. $NAD^+$ levels were quantitated based on the peak area in the chromatograms compared to a standard curve and normalized to tissue weight.

**Glucose Tolerance Test (GTT) and Insulin Tolerance Test (ITT)**

At 8, 10 and 11 weeks of experimental paradigms, mice were subjected to either 12h or 5h of fasting, followed by a glucose tolerance test (GTT) or an insulin tolerance test (ITT) respectively. For the GTT, IP injection of D-glucose (SIGMA cat no. G7021) at 2mg/kg was used, while for ITT, human insulin (Eli Lilly cat. HI0210) at 0.6 U/kg was IP injected. Circulating glucose was measured from a tail-tip blood drop, using an ACCU CHEK active glucometer

(ROCHE) at time points 0 (before injection) and 15, 30, 60 and 120 min after IP injection of either glucose (GTT) or insulin (ITT). Experiments were performed per triplicate, using 5-6 mice per experiment.

**Metabolites and Hormone Analyses**

Blood serum was collected postmortem by cardiac puncture. Triglycerides (TG) in serum and liver were measured using the Triglyceride Colorimetric Assay Kit (Cayman Chemical, cat. no. 10010303). Free fatty acid content was determined with the Free Fatty Acid Fluorometric Assay Kit (Cayman Chemical, cat. no. 700310). Serum insulin and leptin levels were measured by ELISA, using the Ultra-Sensitive Mouse Insulin ELISA Kit (Crystal Chem Inc, cat. no. 90080) and the Mouse Leptin ELISA Kit (Crystal Chem Inc, cat. no. 90030) according to the manufacturer´s instructions. Hepatic cholesterol was determined using a Cholesterol Quantitation Kit (Sigma-Aldrich cat. no. MAK043, colorimetric). Data was collected using a Synergy H1 microplate reader (BioTek).

**Temperature Measurements**

Rectal temperature in mice (n=10 mice, and 3 technical replicates) was registered using a portable digital thermometer (BIOSEB) every 3 hours throughout 24 hours. For the acquisition of infrared thermography, mice were placed inside an acrylic box in darkness. Thermal images were acquired at ZT12 using an Inframetrics C2 Thermal Imaging System Compact Pocket-Size camera (FLIR Systems) with a frequency of 9Hz, thermal sensitivity <0.10 ° C, resolution 80 × 60 (4,800 pixels) and temperature range of 14 to 302 ° F. (n= 4, with 3 technical replicates). Images processing was performed using FLIR-Tools software (2020 FLIR® Systems).

## Oil-Red-O staining

Frozen OCT embedded liver tissues were cut into 10-µm sections using a Leica cryostat and air dried for 10 min at room temperature. Slides were briefly washed with PBS and fixed for 2 min with 4% fresh paraformaldehyde. Preparation of Oil Red O (SIGMA, cat. no.O1391) working solution and staining of slides was performed according to Mehlem *et al* [147]. Oil Red O working solution (3.75 mg/ml) was applied on OCT embedded liver sections for 5 min at RT. Slides were washed twice during 10 min. in water, and mounted in vectashield mounting media (Vector Labs, cat. no. H-1000). The images were captured with the camera Axiocam EEc 5s coupled to a ZEISS Primovert microscope, using a 40X magnification. The background was corrected by white balance and was selected as a blank area outside the section. For representative images, some sections were stained with Gil I haematoxylin. Surface of lipid droplets was quantified using the ImageJ software, by converting RGB to 8-bit grayscale images, and then using the “analyze particles” plug-in to measure the area and size of the lipid drops [148]. Three frames per biopsy were used for image analyses and quantification (n=3 biological replicates with 3 technical replicates).

## SCN dissection

For gene expression analysis from the SCN, frozen brains were placed on ice, and the 1mm$^3$ region above the optic chiasm was dissected out using microscissors. Tissues were placed in microcentrifuge tubes in 100 µl of Trizol and kept at -80°C until use. Total RNA was subsequently extracted and resuspended in 12 µl of water.

## Total RNA extraction

20 mg of liver tissue or the dissected SCN, were homogenized (Benchmark Scientific, D1000 homogenizer) for 30 seconds with 0.5 ml of Trizol (TRIzol™ Reagent, Invitrogen, cat. no.

15596018). The homogenate was incubated for 5 min at RT, then 0.1 ml of chloroform was added, shaken and incubated at RT for 3 min followed by a centrifugation during 15 min at 13,000 rpm at 4 °C. The upper phase was extracted, and 0.25 ml of isopropanol was added. After a 10 min incubation at RT, RNA was precipitated by centrifugation for 10 min at 13,000 rpm and 4 °C. The RNA was washed with 1 ml of 75% ethanol and resuspended in 20 µl of molecular biology grade water (Corning, cat. no. 46-000). 2 µl of the sample were used to quantify its concentration and assess its quality in a NanoDrop (Thermo Scientific)

**cDNA synthesis**

It was performed using the kit iScript™ cDNA synthesis (Bio-Rad, cat. no 1708890). 500 ng of RNA were mixed with 2 µl of 5X iScript Reaction Mix and 0.5 µl of the enzyme iScript Reverse transcriptase in a volume of 10 µl. The thermal cycler (Axygen MaxyGeneTM II) was programmed as follows: Alignment for 5 min at 25 ° C, reverse transcription for 20 min at 46 °C and inactivation for 1 min at 95 °C. The reaction was cooled to 4 °C and diluted to 5 ng/µl.

**Quantitative real-time polymerase chain reaction**

The reactions were performed in a final volume of 10 µl, adding 5 µl of the Universal SYBR Green Super Mix reagent (Bio-Rad, cat. No. 1725121), 1 µl of 2.5 µM forward and reverse primers and 7.5 ng of cDNA per reaction. The thermal cycler (Bio-Rad, CFX96 Touch Real-Time PCR Detection System) was set to the following program: 30s at 95 °C followed by 40 cycles of 5s at 95 °C and 30s at 65 °C. Single-product amplification was verified by an integrated post-run melting curve analysis. Values were normalized to the housekeeping genes *B2m, Ppia* and *Tbp*. The geometric mean was used to determine Ct values of the housekeeping genes and expression values for the genes of interest were calculated using ΔCT methodology. Primer sequences are available in Supplementary Table 4.

## mtDNA Quantification by Quantitative Real-Time PCR

10 mg of liver were used to extract DNA with the DNeasy Blood & Tissue Kit (QIAGEN, cat. no. 69506), according to the manufacturer´s instructions. Quantitative PCR was performed using 7.5 ng of DNA and 2.5 µM of S18 and mtCOX1 primers as described for cDNA quantification, with a program of 20 min at 95°C, followed by 50 to 55 cycles of 15s at 95°C, 20s at 58°C and 20s at 72°C. Single-product amplification was verified by an integrated post-run melting curve analysis. 5-6 mice were analyzed for each time point and condition, with two technical replicates. mtDNA content using the formula: $2\times2^{(\Delta CT)}$,where $\Delta$CT is the difference of CT values between S18 gene and mtCOX1 gene[149].

## Transcriptional profiling from mouse livers

Liver RNA samples for microarray analysis were prepared using our previously described procedures, with slight modifications. Briefly, total RNA was first extracted with TRIzol Reagent (Invitrogen), then cleaned with RNeasy Mini purification Kit (QIAGEN cat. no. 74106) according to the manufacturer's RNA CleanUp protocol. RIN values (≥7.0) were validated with an Agilent Bioanalyzer 2100. 900 ng of total RNA per sample was used as a template to obtain cDNA with the GeneChip cDNA synthesis Kit (Affymetrix, Santa Clara, CA). Microarray experiments were conducted by the Microarray Unit at the National Institute of Genomic Medicine (INMEGEN, Mexico City) using the mouse Clariom™ D Assay (Applied Biosystems™), as per manufacturer´s instructions. Microarray experiments were performed in triplicate (n=3 biological replicates). The Clariom™ D Array consists of 66100 genes (transcript clusters), 214900 transcripts, 498500 exons and 282500 exon-exon splice junctions from *Mus musculus*. Sequences are mapped to the National Center for Biotechnology Information (NCBI) UniGene database. The arrays were scanned in the GeneChip Scanner 3000 7G (Affymetrix) and the

GeneChip Command Console Software was used to obtain the .CEL intensity files. Normalized gene expression data (.CHP files) were obtained with the Transcriptome Analysis Console (TAC v4.0.1.36) software using default parameters. Changes in gene expression (± 1. fold-change; FDR-corrected *p*-value ≤0.05) were subjected to functional analyses using the "Compute Overlaps" tool to explore overlap with the CP (Canonical Pathways) and the GO:BP (GO biological process) gene sets at the MSigDB (molecular signature database). The tool is available at: https://www.gsea-msigdb.org/gsea/msigdb/annotate.jsp, and estimates statistical significance by calculating the FDR q-value. This is the FDR analog of the hypergeometric P-value after correction for multiple hypothesis testing according to Benjamini and Hochberg. Gene set enrichment analysis (GSEA) was performed using GSEA v. 4.0.3. [54] to determine the enrichment score within the Hallmark gene set collection in MSigDB v7.0[150], selecting the Signal2Noise as the metric for ranking genes. The findMotifs.pl program in the HOMER software [151] was used for motif discovery and enrichment, searching within the genomic regions encompassing 300 Kb upstream and 50 Kb downstream the TSS, and selecting 6-8 bp for motif length. Motif enrichment is calculated by findMotifs.pl using the cumulative hypergeometric distribution.

All raw and processed data can be accessed at the GEO database, number: GSE163865.

**Protein carbonyl (PCO) content**

The determination of the carbonyl content was performed from total hepatic protein extracts (0.5 mg/ml), following a previously published protocol [152]. PCO present in the samples were derivatized by reaction with a working solution of 2,4-dinitrophenylhydrazine (DNPH 10 mM diluted in 0.5 M $H_3PO_4$; SIGMA) for 10 min at RT. The reaction was stopped by adding a NaOH (6M) for 10 min. The absorbance of the samples was read in a spectrophotometer

(Jenway, 6305) at 370 nm and the mean absorbance of control tubes (RIPA buffer) was then subtracted. To calculate the PCO concentration expressed as nmol PCO/mg protein, we used the following equation:

$$PCO\ concentration = \frac{10^6 \times \left(\frac{Abs_{366nm}}{22000 M^{-1} * cm^{-1}}\right)}{[protein]_{mg/ml}}$$

**Western Blot**

Livers were lysed in 1X RIPA buffer supplemented with a protease/phosphatase inhibitor cocktail (cOmplete mini ROCHE 1:25 v/v, PMSF 1mM, $Na_3VO_4$ 1mM, NaF 0.5mM). Total protein was quantified with Bradford reagent (SIGMA, cat. no. B6916) and 25 µg of extract were suspended 1:6 (v/v) in 6X Laemmli buffer (60 mM Tris HCl pH 6.8, 12% SDS, 47% glycerol, 0.03% bromophenol blue, 1M DTT), separated on sodium dodecyl sulfate–polyacrylamide gel electrophoresis (SDS-PAGE), and transferred onto PVDF membranes (Merck-Millipore), using the Mini-PROTEAN electrophoretic system (Bio-Rad). Membranes were blocked using non-fat milk in PBST buffer for one hour and incubated with the corresponding primary antibody overnight at 4°C. Membranes were washed three times with PBST and incubated with the secondary antibody for 5 hrs at RT. Antibodies used in this study were: From Cell Signaling: PPARγ (2443), AKT (9272), Phospho-AKT$_{Ser473}$ (9271), AMPKα (5831), Phospho-AMPKα$_{Thr172}$ (50081), mTOR (2893), ), Phospho-mTOR$_{Ser2448}$ (5536), Phospho-p70 S6K$_{Thr389}$ (9234), Phospho-4E-BP1$_{Thr37/46}$ (2855), RSK1/RSK2/RSK3 (9355), Phospho-p90RSK$_{Ser359}$ (8753), REV-ERBα (13418), ULK1 (8054), Phospho-ULK1$_{Ser555}$ (5869), all diluted 1:1000; from Santa Cruz: C/EBPα (SC-365318, 1:500); from Abcam: BMAL1 (Ab3350, 1:1000); from Alpha Diagnostics International: PER2 (PER21-A 1:2000); from Bethyl Laboratories: CRY1 (A302-614A 1:1000); from Sigma: α-Tubulin (T5168, 1:80000); from

Genetex: GAPDH-HRP (GTX627408-01, 1:120000) and P84 (GTX70220-01, 1:1000) The secondary antibodies were Anti-rabbit IgG (Cell Signaling, 7074, 1:150000 for BMAL1, 1:10000 for Pparγ and 1:80000 for the rest) or Anti-mouse IgG (Sigma I8765, 1:80000), conjugated to horseradish peroxidase. For detection, the Immobilon Western Chemiluminescent HRP Substrate (Millipore, cat. no. WBKLS0100) was used and luminescence was visualized and documented in a Gel Logic 1500 Imaging System (KODAK). Protein bands were quantified by densitometric analysis using Image Studio Lite Version 5.0 software (LI-COR biosciences). 4-5 biological replicates were used for each quantification.

**Chromatin immunoprecipitation (ChIP)**

100-200 mg of liver tissue were homogenized with a pestle in PBS. Dual crosslinking was performed in a final volume of 1ml using 2 mM of DSG (Disuccinimidyl glutarate, ProteoChem, CAS: 79642-50-5) for 10 min at RT on a rotary shaker. DSG was washed out and a second crosslink was performed using 1% formaldehyde (Sigma-Aldrich, F8775) in PBS for 15 min at RT on a rotary shaker. Crosslinking was stopped with 0.125 M glycine for 5 min at 4°C. After two washes with ice-cold PBS, nuclei were isolated by resuspending the tissue in 600 µL of ice-cold nuclei preparation buffer (NPB: 10 mM HEPES, 10 mM KCl, 1.5 mM MgCl2, 250 mM sucrose, 0.1% IGEPAL CA-630) and incubating at 4°C for 5 min in rotation. Nuclei were collected by centrifugation at 1,500g for 12 min at 4°C and, and resuspended in 600 µL of cold nuclear lysis buffer (10 mM Tris pH 8, 1 mM EDTA, 0.5 mM EGTA, 0.3% SDS, 1X cOmplete™ Protease Inhibitor Cocktail, Roche) for 30 min on ice. Nuclear lysates were stored at -80°C. 300 µL of lysates were sonicated using a Bioruptor Pico Sonicator (Diagenode) for 15 cycles (30 s ON/30 s OFF). Chromatin fragments (100-500 bp) were evaluated on agarose gels using 10 µL of sonicated chromatin for DNA purification using the phenol method. 600 µL of ice-cold

ChIP-dilution buffer (1% Triton X-100, 2 mM EDTA, 20 mM Tris pH 8, 150 mM NaCl, 1 mM PMSF, 1X cOmplete™ Protease Inhibitor Cocktail, Roche) was added to the fragmented chromatin, and 10% volume was recovered as the Input. Immunoprecipitation was set up overnight at 4ºC, by adding 20 µL of magnetic beads (Magna ChIP Protein G Magnetic Beads C #16-662, Sigma-Aldrich) and a combination of two anti BMAL1 antibodies: 1.25 µL rabbit anti-BMAL1 (ab3350, Abcam) and 2.5 µL rabbit anti-BMAL1 (ab93806, Abcam). Immunoprecipitations with 4 µL of normal mouse IgG (Sigma-Aldrich, Cat. No. 18765) were performed simultaneously. Sequential washes of the magnetic beads were performed for 10 min at 4°C, as follows: Wash buffer 1 (20 mM Tris pH 8, 0.1% SDS, 1% Triton X-100, 150 mM NaCl, 2 mM EDTA), Wash buffer 2 (20 mM Tris pH 8, 0.1% SDS, 1% Triton X-100, 500 mM NaCl, 2 mM EDTA), Wash buffer 3 (10 mM Tris pH 8, 250 mM LiCl, 1% IGEPAL CA-630, 1% sodium deoxycolate) and TE buffer (10 mM Tris pH 8, 1 mM EDTA). Chromatin was eluted by adding 400 µL of fresh elution buffer (10 mM Tris pH 8, 0.5% SDS, 300 mM NaCl, 5 mM EDTA, 0.05 mg/mL proteinase K) to the magnetic beads and incubating overnight at 65°C. A treatment with RNase A at 0.1 mg/ml for 30 min at 37 °C was performed. The DNA was purified from the IPs and Inputs by adding one volume of phenol:chloroform:isoamamyl alcohol (25:24:1). After mixing and centrifugation, the aqueous phase was recovered, and DNA was precipitated by adding 1/10 volumes of sodium acetate (0.3 M pH 5.2), 20 µg of glycogen (10901393001, Roche) and 2 volumes of ice-cold ethanol, at -80°C overnight. DNA was pelleted by centrifugation at 13500 rpm for 30 min at 4°C. The DNA was washed with 70% ethanol, and resuspended in 50 µL of molecular grade water. 1.5 µl were used for subsequent qRT-PCR reactions with specific primers designed using Primer3web, within regulatory regions

858 previously identified as BMAL1 binding sites in mouse liver, as reported in the ChIP-Atlas
859 database[153]. Primer sequences are available in Supplementary Table S4.

860 **Assessment of locomotor behavior**

861 Mice were individually housed in a light-tight, ventilated cabinet, under a 12h light:12h dark
862 cycle, and ad libitum access to food and water. At the appropriate time for each treatment,
863 animals were removed from their cages to receive IP injections for less than 2 minutes each.
864 Cages were equipped with two infrared motion sensors (OASPAD system, OMNIALVA). Beam
865 break data was continuously recorded and compiled with the OASPAD20 (OMNIALVA)
866 software, and files containing the number of beam breaks per 6-minute bin were exported.
867 Double-plotted actograms were generated using RhythmicAlly [154]. Activity profiles were
868 obtained averaging 5 consecutive days prior to the $NAD^+$ treatment, and 5 consecutive days
869 after the start of the treatment. Activity profile data from 30 minutes were averaged for
870 statistical comparisons.

871 **Statistical analyses**

872 All data was presented as the mean ± standard error of the mean, and two-way analysis of
873 variance (ANOVA) followed by Tukey's test for multiple comparisons was used for statistical
874 analyses except when otherwise noted in the figure legends. Differences between groups were
875 rated as statistically significant at $P < 0.05$. GraphPad Prism version 5.0 for Windows
876 (GraphPad Software Inc., San Diego, CA, USA) and Excel (Microsoft Office 360) were used for
877 statistical analyses and plotting. 24-hours period rhythms were assessed employing CircWave
878 version 1.4 [155], CircWave uses a forward linear harmonic regression to calculate the profile of
879 the wave fitted into a 24h period. Daily rhythms were confirmed when the null amplitude
880 hypothesis was rejected by running an *F* test that produced a significant value ($P<0.05$).

CircWave provides the calculation of the Centre of Gravity (CoG), representing the acrophase of the curve, with SD. Double-plotted data (ZT24) for visualization proposes are indicated in figure legends, and were not included in the statistical analyses. Figures were assembled using Adobe Illustrator CC 2015 (Adobe Inc., San José, CA, USA).

**Data availability:** All data generated or analyzed during this study are included in this article (and its supplementary information files). Source data are provided with this paper. All gene expression data that support the findings of this study have been deposited in the National Center for Biotechnology Information Gene Expression Omnibus (GEO) and are accessible through the GEO Series accession number: GSE163865.

## REFERENCES

1 Blüher, M. Obesity: global epidemiology and pathogenesis. *Nature Reviews Endocrinology* **15**, 288-298, (2019).
2 Kahn, S. E., Cooper, M. E. & Del Prato, S. Pathophysiology and treatment of type 2 diabetes: perspectives on the past, present, and future. *Lancet* **383**, 1068-1083, (2014).
3 Heymsfield, S. B. & Wadden, T. A. Mechanisms, Pathophysiology, and Management of Obesity. *New England Journal of Medicine* **376**, 254-266, (2017).
4 Peeples, L. Medicine's secret ingredient - it's in the timing. *Nature* **556**, 290-292, (2018).
5 Kathale, N. D. & Liu, A. C. Prevalence of cycling genes and drug targets calls for prospective chronotherapeutics. *Proceedings of the National Academy of Sciences* **111**, 15869-15870, (2014).
6 Zhang, R., Lahens, N. F., Ballance, H. I., Hughes, M. E. & Hogenesch, J. B. A circadian gene expression atlas in mammals: Implications for biology and medicine. *Proceedings of the National Academy of Sciences* **111**, 16219-16224, (2014).
7 Ruben, M. D., Smith, D. F., FitzGerald, G. A. & Hogenesch, J. B. Dosing time matters. *Science* **365**, 547-549, (2019).
8 Münch, M. & Kramer, A. Timing matters: New tools for personalized chronomedicine and circadian health. *Acta Physiologica* **227**, e13300, (2019).
9 Dibner, C., Schibler, U. & Albrecht, U. The Mammalian Circadian Timing System: Organization and Coordination of Central and Peripheral Clocks. *Annual Review of Physiology* **72**, 517-549, (2010).
10 Crnko, S., Du Pré, B. C., Sluijter, J. P. G. & Van Laake, L. W. Circadian rhythms and the molecular clock in cardiovascular biology and disease. *Nature Reviews Cardiology* **16**, 437-447, (2019).
11 Qian, J. & Scheer, F. A. J. L. Circadian System and Glucose Metabolism: Implications for Physiology and Disease. *Trends in Endocrinology & Metabolism* **27**, 282-293, (2016).

914 12 Zimmet, P. *et al.* The Circadian Syndrome: is the Metabolic Syndrome and much more! *J Intern Med* **286**, 181-191, (2019).
916 13 Takahashi, J. S. Transcriptional architecture of the mammalian circadian clock. *Nature Reviews Genetics* **18**, 164-179, (2017).
918 14 Pacheco-Bernal, I., Becerril-Pérez, F. & Aguilar-Arnal, L. Circadian rhythms in the three-dimensional genome: implications of chromatin interactions for cyclic transcription. *Clinical epigenetics* **11**, 79, (2019).
921 15 Dyar, K. A. *et al.* Atlas of Circadian Metabolism Reveals System-wide Coordination and Communication between Clocks. *Cell* **174**, 1571-1585.e1511, (2018).
923 16 Eckel-Mahan, K. L. *et al.* Reprogramming of the circadian clock by nutritional challenge. *Cell* **155**, 1464-1478, (2013).
925 17 Hatori, M. *et al.* Time-Restricted Feeding without Reducing Caloric Intake Prevents Metabolic Diseases in Mice Fed a High-Fat Diet. *Cell metabolism* **15**, 848-860, (2012).
927 18 Dallmann, R., Viola, A. U., Tarokh, L., Cajochen, C. & Brown, S. A. The human circadian metabolome. *Proceedings of the National Academy of Sciences* **109**, 2625-2629, (2012).
929 19 Nakahata, Y., Sahar, S., Astarita, G., Kaluzova, M. & Sassone-Corsi, P. Circadian control of the NAD+ salvage pathway by CLOCK-SIRT1. *Science* **324**, 654-657, (2009).
931 20 Ramsey, K. M. *et al.* Circadian clock feedback cycle through NAMPT-mediated NAD+ biosynthesis. *Science* **324**, 651-654, (2009).
933 21 Peek, C. B. *et al.* Circadian clock NAD+ cycle drives mitochondrial oxidative metabolism in mice. *Science* **342**, 1243417-1243417, (2013).
935 22 Jacobi, D. *et al.* Hepatic Bmal1 Regulates Rhythmic Mitochondrial Dynamics and Promotes Metabolic Fitness. *Cell metabolism* **22**, 709-720, (2015).
937 23 Neufeld-Cohen, A. *et al.* Circadian control of oscillations in mitochondrial rate-limiting enzymes and nutrient utilization by PERIOD proteins. *Proceedings of the National Academy of Sciences* **113**, E1673-E1682, (2016).
940 24 Scrima, R. *et al.* Clock-genes and mitochondrial respiratory activity: Evidence of a reciprocal interplay. *Biochimica et Biophysica Acta (BBA) - Bioenergetics* **1857**, 1344-1351, (2016).
942 25 de Goede, P., Wefers, J., Brombacher, E. C., Schrauwen, P. & Kalsbeek, A. Circadian rhythms in mitochondrial respiration. *J Mol Endocrinol* **60**, R115-R130, (2018).
944 26 Koronowski, K. B. *et al.* Defining the Independence of the Liver Circadian Clock. *Cell* **177**, 1448-1462.e1414, (2019).
946 27 Sato, S. *et al.* Circadian Reprogramming in the Liver Identifies Metabolic Pathways of Aging. *Cell* **170**, 664-677.e611, (2017).
948 28 Reinke, H. & Asher, G. Crosstalk between metabolism and circadian clocks. *Nature Reviews Molecular Cell Biology* **20**, 227-241, (2019).
950 29 Yang, Y. & Sauve, A. A. NAD(+) metabolism: Bioenergetics, signaling and manipulation for therapy. *Biochimica et biophysica acta* **1864**, 1787-1800, (2016).
952 30 Bogan, K. L. & Brenner, C. Nicotinic acid, nicotinamide, and nicotinamide riboside: a molecular evaluation of NAD+ precursor vitamins in human nutrition. *Annual review of nutrition* **28**, 115-130, (2008).
955 31 Teodoro, J. S., Rolo, A. P. & Palmeira, C. M. The NAD ratio redox paradox: why does too much reductive power cause oxidative stress? *Toxicology mechanisms and methods* **23**, 297-302, (2013).
957 32 Gariani, K. *et al.* Eliciting the mitochondrial unfolded protein response by nicotinamide adenine dinucleotide repletion reverses fatty liver disease in mice. *Hepatology* **63**, 1190-1204, (2016).
959 33 Gulshan, M. *et al.* Overexpression of Nmnat3 efficiently increases NAD and NGD levels and ameliorates age-associated insulin resistance. *Aging Cell* **17**, e12798, (2018).

34 Liu, S., Kim, T.-H., Franklin, D. A. & Zhang, Y. Protection against High-Fat-Diet-Induced Obesity in MDM2<sup>C305F</sup> Mice Due to Reduced p53 Activity and Enhanced Energy Expenditure. *Cell Reports* **18**, 1005-1018, (2017).

35 Trammell, S. A. J. *et al.* Nicotinamide Riboside Opposes Type 2 Diabetes and Neuropathy in Mice. *Scientific Reports* **6**, 26933, (2016).

36 Yoshino, J., Mills, K. F., Yoon, M. J. & Imai, S. Nicotinamide mononucleotide, a key NAD(+) intermediate, treats the pathophysiology of diet- and age-induced diabetes in mice. *Cell metabolism* **14**, 528-536, (2011).

37 Jukarainen, S. *et al.* Obesity is associated with low NAD+/SIRT pathway expression in adipose tissue of BMI-discordant monozygotic twins. *The Journal of Clinical Endocrinology* **101**, 275-283, (2016).

38 Matasic, D. S., Brenner, C. & London, B. Emerging potential benefits of modulating NAD(+) metabolism in cardiovascular disease. *American journal of physiology. Heart and circulatory physiology* **314**, H839-H852, (2018).

39 Zapata-Perez, R., Wanders, R. J. A., van Karnebeek, C. D. M. & Houtkooper, R. H. NAD(+) homeostasis in human health and disease. *EMBO molecular medicine* **13**, e13943, (2021).

40 Cantó, C. *et al.* The NAD+ precursor nicotinamide riboside enhances oxidative metabolism and protects against high-fat diet-induced obesity. *Cell metabolism* **15**, 838-847, (2012).

41 Mitchell, S. J. *et al.* Nicotinamide Improves Aspects of Healthspan, but Not Lifespan, in Mice. *Cell metabolism* **27**, 667-676.e664, (2018).

42 Pham, T. X. *et al.* Nicotinamide riboside, an NAD+ precursor, attenuates the development of liver fibrosis in a diet-induced mouse model of liver fibrosis. *Biochimica et Biophysica Acta (BBA) - Molecular Basis of Disease* **1865**, 2451-2463, (2019).

43 Sambeat, A. *et al.* Endogenous nicotinamide riboside metabolism protects against diet-induced liver damage. *Nature Communications* **10**, 4291, (2019).

44 Zhou, C.-C. *et al.* Hepatic NAD+ deficiency as a therapeutic target for non-alcoholic fatty liver disease in ageing. *British Journal of Pharmacology* **173**, 2352-2368, (2016).

45 Yoshino, M. *et al.* Nicotinamide mononucleotide increases muscle insulin sensitivity in prediabetic women. *Science* **372**, 1224-1229, (2021).

46 Levine, D. C. *et al.* NAD+ Controls Circadian Reprogramming through PER2 Nuclear Translocation to Counter Aging. *Molecular Cell* **78**, 835-849.e837, (2020).

47 Kohsaka, A. *et al.* High-fat diet disrupts behavioral and molecular circadian rhythms in mice. *Cell metabolism* **6**, 414-421, (2007).

48 Orozco-Solis, R. *et al.* The Circadian Clock in the Ventromedial Hypothalamus Controls Cyclic Energy Expenditure. *Cell metabolism* **23**, 467-478, (2016).

49 Stenvers, D. J., Scheer, F., Schrauwen, P., la Fleur, S. E. & Kalsbeek, A. Circadian clocks and insulin resistance. *Nature Reviews Endocrinology* **15**, 75-89, (2019).

50 Lefterova, M. I., Haakonsson, A. K., Lazar, M. A. & Mandrup, S. PPARγ and the global map of adipogenesis and beyond. *Trends in endocrinology and metabolism: TEM* **25**, 293-302, (2014).

51 Rosen, E. D. *et al.* C/EBPalpha induces adipogenesis through PPARgamma: a unified pathway. *Genes & development* **16**, 22-26, (2002).

52 Clarke, S. L., Robinson, C. E. & Gimble, J. M. CAAT/enhancer binding proteins directly modulate transcription from the peroxisome proliferator-activated receptor gamma 2 promoter. *Biochemical and biophysical research communications* **240**, 99-103, (1997).

53 Krishnaiah, S. Y. *et al.* Clock Regulation of Metabolites Reveals Coupling between Transcription and Metabolism. *Cell metabolism* **25**, 961-974.e964, (2017).

54 Subramanian, A. *et al.* Gene set enrichment analysis: A knowledge-based approach for interpreting genome-wide expression profiles. *Proceedings of the National Academy of Sciences* **102**, 15545-15550, (2005).

55 Cai, D. *et al.* Local and systemic insulin resistance resulting from hepatic activation of IKK-beta and NF-kappaB. *Nature medicine* **11**, 183-190, (2005).

56 Asrih, M. & Jornayvaz, F. R. Inflammation as a potential link between nonalcoholic fatty liver disease and insulin resistance. *Journal of Endocrinology* **218**, R25, (2013).

57 Bochkis, I. M. *et al.* Hepatocyte-specific ablation of Foxa2 alters bile acid homeostasis and results in endoplasmic reticulum stress. *Nature medicine* **14**, 828-836, (2008).

58 Wolfrum, C., Asilmaz, E., Luca, E., Friedman, J. M. & Stoffel, M. Foxa2 regulates lipid metabolism and ketogenesis in the liver during fasting and in diabetes. *Nature* **432**, 1027-1032, (2004).

59 Manning, B. D. & Toker, A. AKT/PKB Signaling: Navigating the Network. *Cell* **169**, 381-405, (2017).

60 Vollmers, C. *et al.* Time of feeding and the intrinsic circadian clock drive rhythms in hepatic gene expression. *Proceedings of the National Academy of Sciences* **106**, 21453-21458, (2009).

61 Lamia, K. A. *et al.* AMPK regulates the circadian clock by cryptochrome phosphorylation and degradation. *Science* **326**, 437-440, (2009).

62 Mihaylova, M. M. & Shaw, R. J. The AMPK signalling pathway coordinates cell growth, autophagy and metabolism. *Nature Cell Biology* **13**, 1016-1023, (2011).

63 Robles, M. S., Humphrey, S. J. & Mann, M. Phosphorylation Is a Central Mechanism for Circadian Control of Metabolism and Physiology. *Cell metabolism* **25**, 118-127, (2017).

64 Jouffe, C. *et al.* The Circadian Clock Coordinates Ribosome Biogenesis. *PLOS Biology* **11**, e1001455, (2013).

65 Roux, P. P. & Topisirovic, I. Regulation of mRNA translation by signaling pathways. *Cold Spring Harb Perspect Biol* **4**, a012252, (2012).

66 Carrière, A. *et al.* Oncogenic MAPK Signaling Stimulates mTORC1 Activity by Promoting RSK-Mediated Raptor Phosphorylation. *Current Biology* **18**, 1269-1277, (2008).

67 Hutagalung, A. H. & Novick, P. J. Role of Rab GTPases in membrane traffic and cell physiology. *Physiol Rev* **91**, 119-149, (2011).

68 Zoppino, F. C., Militello, R. D., Slavin, I., Alvarez, C. & Colombo, M. I. Autophagosome formation depends on the small GTPase Rab1 and functional ER exit sites. *Traffic (Copenhagen, Denmark)* **11**, 1246-1261, (2010).

69 Hyttinen, J. M. T., Niittykoski, M., Salminen, A. & Kaarniranta, K. Maturation of autophagosomes and endosomes: A key role for Rab7. *Biochimica et Biophysica Acta (BBA) - Molecular Cell Research* **1833**, 503-510, (2013).

70 Ao, X., Zou, L. & Wu, Y. Regulation of autophagy by the Rab GTPase network. *Cell Death & Differentiation* **21**, 348-358, (2014).

71 Li, Z. *et al.* A novel Rab10-EHBP1-EHD2 complex essential for the autophagic engulfment of lipid droplets. *Science advances* **2**, e1601470-e1601470, (2016).

72 Ayala, C. I., Kim, J. & Neufeld, T. P. Rab6 promotes insulin receptor and cathepsin trafficking to regulate autophagy induction and activity in Drosophila. *J Cell Sci* **131**, jcs216127, (2018).

73 Sun, Y., Bilan, P. J., Liu, Z. & Klip, A. Rab8A and Rab13 are activated by insulin and regulate GLUT4 translocation in muscle cells. *Proc Natl Acad Sci U S A* **107**, 19909-19914, (2010).

74 Chong, C.-M. *et al.* Presenilin 1 deficiency suppresses autophagy in human neural stem cells through reducing γ-secretase-independent ERK/CREB signaling. *Cell Death & Disease* **9**, 879, (2018).

75 Wolf, E. *et al.* Miz1 is required to maintain autophagic flux. *Nature Communications* **4**, 2535, (2013).

76 Xiong, Q. *et al.* Nr2e1 ablation impairs liver glucolipid metabolism and induces inflammation, high-fat diets amplify the damage. *Biomedicine & Pharmacotherapy* **120**, 109503, (2019).

77 Hayhurst, G. P., Lee, Y. H., Lambert, G., Ward, J. M. & Gonzalez, F. J. Hepatocyte nuclear factor 4alpha (nuclear receptor 2A1) is essential for maintenance of hepatic gene expression and lipid homeostasis. *Molecular and cellular biology* **21**, 1393-1403, (2001).

78 Zhan, Y.-y. *et al.* The orphan nuclear receptor Nur77 regulates LKB1 localization and activates AMPK. *Nature Chemical Biology* **8**, 897-904, (2012).
79 Thomas, D. D., Corkey, B. E., Istfan, N. W. & Apovian, C. M. Hyperinsulinemia: An Early Indicator of Metabolic Dysfunction. *Journal of the Endocrine Society* **3**, 1727-1747, (2019).
80 Lavigne, P. M. & Karas, R. H. The Current State of Niacin in Cardiovascular Disease Prevention: A Systematic Review and Meta-Regression. *Journal of the American College of Cardiology* **61**, 440-446, (2013).
81 Romani, M., Hofer, D. C., Katsyuba, E. & Auwerx, J. Niacin: an old lipid drug in a new NAD(+) dress. *J Lipid Res* **60**, 741-746, (2019).
82 Merrill, G. F., Kurth, E. J., Hardie, D. G. & Winder, W. W. AICA riboside increases AMP-activated protein kinase, fatty acid oxidation, and glucose uptake in rat muscle. *The American journal of physiology* **273**, E1107-1112, (1997).
83 Yoshino, J., Baur, J. A. & Imai, S. I. NAD(+) Intermediates: The Biology and Therapeutic Potential of NMN and NR. *Cell metabolism* **27**, 513-528, (2018).
84 Guan, D. *et al.* Diet-Induced Circadian Enhancer Remodeling Synchronizes Opposing Hepatic Lipid Metabolic Processes. *Cell* **174**, 831-842.e812, (2018).
85 Beattie, J. H. *et al.* Obesity and hyperleptinemia in metallothionein (-I and -II) null mice. *Proceedings of the National Academy of Sciences* **95**, 358-363, (1998).
86 Sato, M. *et al.* Development of high-fat-diet-induced obesity in female metallothionein-null mice. *The FASEB Journal* **24**, 2375-2384, (2010).
87 Swindell, W. R. Metallothionein and the biology of aging. *Ageing Research Reviews* **10**, 132-145, (2011).
88 Xu, Y. *et al.* Lipocalin-2 Protects Against Diet-Induced Nonalcoholic Fatty Liver Disease by Targeting Hepatocytes. *Hepatology Communications* **3**, 763-775, (2019).
89 Rutter, J., Reick, M., Wu, L. C. & McKnight, S. L. Regulation of clock and NPAS2 DNA binding by the redox state of NAD cofactors. *Science* **293**, 510-514, (2001).
90 Koike, N. *et al.* Transcriptional architecture and chromatin landscape of the core circadian clock in mammals. *Science* **338**, 349-354, (2012).
91 Damiola, F. *et al.* Restricted feeding uncouples circadian oscillators in peripheral tissues from the central pacemaker in the suprachiasmatic nucleus. *Genes & development* **14**, 2950-2961, (2000).
92 Saini, C. *et al.* Real-time recording of circadian liver gene expression in freely moving mice reveals the phase-setting behavior of hepatocyte clocks. *Genes & development* **27**, 1526-1536, (2013).
93 de Guia, R. M. *et al.* Fasting- and ghrelin-induced food intake is regulated by NAMPT in the hypothalamus. *Acta Physiol (Oxf)* **228**, e13437, (2020).
94 Roh, E. *et al.* Effects of Chronic NAD Supplementation on Energy Metabolism and Diurnal Rhythm in Obese Mice. *Obesity* **26**, 1448-1456, (2018).
95 Schein, P. S. & Loftus, S. Streptozotocin: depression of mouse liver pyridine nucleotides. *Cancer research* **28**, 1501-1506, (1968).
96 Rajman, L., Chwalek, K. & Sinclair, D. A. Therapeutic Potential of NAD-Boosting Molecules: The In Vivo Evidence. *Cell metabolism* **27**, 529-547, (2018).
97 Belenky, P., Bogan, K. L. & Brenner, C. NAD+ metabolism in health and disease. *Trends in Biochemical Sciences* **32**, 12-19, (2007).
98 Bieganowski, P. & Brenner, C. Discoveries of Nicotinamide Riboside as a Nutrient and Conserved NRK Genes Establish a Preiss-Handler Independent Route to NAD+ in Fungi and Humans. *Cell* **117**, 495-502, (2004).
99 Ratajczak, J. *et al.* NRK1 controls nicotinamide mononucleotide and nicotinamide riboside metabolism in mammalian cells. *Nat Commun* **7**, 13103, (2016).

100 Nikiforov, A., Dolle, C., Niere, M. & Ziegler, M. Pathways and subcellular compartmentation of NAD biosynthesis in human cells: from entry of extracellular precursors to mitochondrial NAD generation. *The Journal of biological chemistry* **286**, 21767-21778, (2011).
101 Liu, L. *et al.* Quantitative Analysis of NAD Synthesis-Breakdown Fluxes. *Cell metabolism* **27**, 1067-1080.e1065, (2018).
102 Kory, N. *et al.* MCART1/SLC25A51 is required for mitochondrial NAD transport. *Science Advances* **6**, eabe5310, (2020).
103 Luongo, T. S. *et al.* SLC25A51 is a mammalian mitochondrial NAD+ transporter. *Nature*, (2020).
104 Aguilar-Arnal, L. *et al.* Spatial dynamics of SIRT1 and the subnuclear distribution of NADH species. *Proceedings of the National Academy of Sciences* **113**, 12715-12720, (2016).
105 Billington, R. A. *et al.* Characterization of NAD uptake in mammalian cells. *The Journal of biological chemistry* **283**, 6367-6374, (2008).
106 Rey, G. *et al.* The Pentose Phosphate Pathway Regulates the Circadian Clock. *Cell metabolism* **24**, 462-473, (2016).
107 Caton, P. W., Kieswich, J., Yaqoob, M. M., Holness, M. J. & Sugden, M. C. Nicotinamide mononucleotide protects against pro-inflammatory cytokine-mediated impairment of mouse islet function. *Diabetologia* **54**, 3083-3092, (2011).
108 Uddin, G. M., Youngson, N. A., Sinclair, D. A. & Morris, M. J. Head to Head Comparison of Short-Term Treatment with the NAD(+) Precursor Nicotinamide Mononucleotide (NMN) and 6 Weeks of Exercise in Obese Female Mice. *Frontiers in pharmacology* **7**, 258, (2016).
109 Lee, H. J., Hong, Y. S., Jun, W. & Yang, S. J. Nicotinamide Riboside Ameliorates Hepatic Metaflammation by Modulating NLRP3 Inflammasome in a Rodent Model of Type 2 Diabetes. *Journal of medicinal food* **18**, 1207-1213, (2015).
110 Mukherjee, S. *et al.* Nicotinamide adenine dinucleotide biosynthesis promotes liver regeneration. *Hepatology* **65**, 616-630, (2017).
111 Shi, W. *et al.* Effects of a wide range of dietary nicotinamide riboside (NR) concentrations on metabolic flexibility and white adipose tissue (WAT) of mice fed a mildly obesogenic diet. *Molecular nutrition & food research* **61**, (2017).
112 Peng, C. *et al.* RSK2 mediates NF-{kappa}B activity through the phosphorylation of IkappaBalpha in the TNF-R1 pathway. *FASEB J* **24**, 3490-3499, (2010).
113 Shahbazian, D. *et al.* The mTOR/PI3K and MAPK pathways converge on eIF4B to control its phosphorylation and activity. *The EMBO Journal* **25**, 2781-2791, (2006).
114 González, A., Hall, M. N., Lin, S.-C. & Hardie, D. G. AMPK and TOR: The Yin and Yang of Cellular Nutrient Sensing and Growth Control. *Cell metabolism* **31**, 472-492, (2020).
115 Dalle Pezze, P. *et al.* A systems study reveals concurrent activation of AMPK and mTOR by amino acids. *Nature Communications* **7**, 13254, (2016).
116 Day, E. A., Ford, R. J. & Steinberg, G. R. AMPK as a Therapeutic Target for Treating Metabolic Diseases. *Trends in endocrinology and metabolism: TEM* **28**, 545-560, (2017).
117 Wong, Aaron K. F., Howie, J., Petrie, John R. & Lang, Chim C. AMP-activated protein kinase pathway: a potential therapeutic target in cardiometabolic disease. *Clinical Science* **116**, 607-620, (2009).
118 Lamia, K. A. *et al.* AMPK Regulates the Circadian Clock by Cryptochrome Phosphorylation and Degradation. *Science* **326**, 437-440, (2009).
119 Stokkan, K. A., Yamazaki, S., Tei, H., Sakaki, Y. & Menaker, M. Entrainment of the circadian clock in the liver by feeding. *Science* **291**, 490-493, (2001).
120 Aguilar-Arnal, L., Katada, S., Orozco-Solis, R. & Sassone-Corsi, P. NAD(+)-SIRT1 control of H3K4 trimethylation through circadian deacetylation of MLL1. *Nature structural & molecular biology* **22**, 312-318, (2015).

121 Fang, B. *et al.* Circadian Enhancers Coordinate Multiple Phases of Rhythmic Gene Transcription In Vivo. *Cell* **159**, 1140-1152, (2014).
122 Bruce, K. D., Zsombok, A. & Eckel, R. H. Lipid Processing in the Brain: A Key Regulator of Systemic Metabolism. *Frontiers in Endocrinology* **8**, (2017).
123 Menet, J. S., Pescatore, S. & Rosbash, M. CLOCK:BMAL1 is a pioneer-like transcription factor. *Genes & development* **28**, 8-13, (2014).
124 Rey, G. *et al.* Genome-Wide and Phase-Specific DNA-Binding Rhythms of BMAL1 Control Circadian Output Functions in Mouse Liver. *PLOS Biology* **9**, e1000595, (2011).
125 Qu, M., Qu, H., Jia, Z. & Kay, S. A. HNF4A defines tissue-specific circadian rhythms by beaconing BMAL1::CLOCK chromatin binding and shaping the rhythmic chromatin landscape. *Nature Communications* **12**, 6350, (2021).
126 Beytebiere, J. R. *et al.* Tissue-specific BMAL1 cistromes reveal that rhythmic transcription is associated with rhythmic enhancer–enhancer interactions. *Genes & development* **33**, 294-309, (2019).
127 Katsyuba, E., Romani, M., Hofer, D. & Auwerx, J. NAD+ homeostasis in health and disease. *Nature Metabolism* **2**, 9-31, (2020).
128 Asher, G. *et al.* SIRT1 Regulates Circadian Clock Gene Expression through PER2 Deacetylation. *Cell* **134**, 317-328, (2008).
129 Nakahata, Y. *et al.* The NAD+-dependent deacetylase SIRT1 modulates CLOCK-mediated chromatin remodeling and circadian control. *Cell* **134**, 329-340, (2008).
130 Picard, F. *et al.* Sirt1 promotes fat mobilization in white adipocytes by repressing PPAR-gamma. *Nature* **429**, 771-776, (2004).
131 Baron, K. G. & Reid, K. J. Circadian misalignment and health. *International review of psychiatry* **26**, 139-154, (2014).
132 Leproult, R., Holmback, U. & Van Cauter, E. Circadian misalignment augments markers of insulin resistance and inflammation, independently of sleep loss. *Diabetes* **63**, 1860-1869, (2014).
133 Wefers, J. *et al.* Circadian misalignment induces fatty acid metabolism gene profiles and compromises insulin sensitivity in human skeletal muscle. *Proc Natl Acad Sci U S A* **115**, 7789-7794, (2018).
134 Hara, R. *et al.* Restricted feeding entrains liver clock without participation of the suprachiasmatic nucleus. *Genes to cells : devoted to molecular & cellular mechanisms* **6**, 269-278, (2001).
135 Mukherji, A., Kobiita, A. & Chambon, P. Shifting the feeding of mice to the rest phase creates metabolic alterations, which, on their own, shift the peripheral circadian clocks by 12 hours. *Proc Natl Acad Sci U S A* **112**, E6683-6690, (2015).
136 Huang, Q. *et al.* Combination of NAD(+) and NADPH Offers Greater Neuroprotection in Ischemic Stroke Models by Relieving Metabolic Stress. **55**, 6063-6075, (2018).
137 Roh, E. *et al.* Exogenous nicotinamide adenine dinucleotide regulates energy metabolism via hypothalamic connexin 43. *Metabolism: clinical and experimental* **88**, 51-60, (2018).
138 Covarrubias, A. J. *et al.* Senescent cells promote tissue NAD(+) decline during ageing via the activation of CD38(+) macrophages. *Nat Metab* **2**, 1265-1283, (2020).
139 Chini, C. C. S. *et al.* CD38 ecto-enzyme in immune cells is induced during aging and regulates NAD(+) and NMN levels. *Nat Metab* **2**, 1284-1304, (2020).
140 Droin, C. *et al.* Space-time logic of liver gene expression at sub-lobular scale. *Nat Metab* **3**, 43-58, (2021).
141 Tullius, S. G. *et al.* NAD+ protects against EAE by regulating CD4+ T-cell differentiation. *Nat Commun* **5**, 5101, (2014).
142 Wang, J. *et al.* Treatment with NAD(+) inhibited experimental autoimmune encephalomyelitis by activating AMPK/SIRT1 signaling pathway and modulating Th1/Th17 immune responses in mice. *International immunopharmacology* **39**, 287-294, (2016).
143 Liu, B., Zhao, G., Jin, L. & Shi, J. Nicotinamide Improves Cognitive Function in Mice With Chronic Cerebral Hypoperfusion. *Frontiers in neurology* **12**, 596641, (2021).

144 Wang, C. *et al.* Nicotinamide Administration Improves Remyelination after Stroke. *Neural plasticity* **2017**, 7019803, (2017).
145 Zheng, M. *et al.* Nicotinamide reduces renal interstitial fibrosis by suppressing tubular injury and inflammation. *Journal of cellular and molecular medicine* **23**, 3995-4004, (2019).
146 Yoshino, J. & Imai, S. Accurate measurement of nicotinamide adenine dinucleotide (NAD(+)) with high-performance liquid chromatography. *Methods in molecular biology* **1077**, 203-215, (2013).
147 Mehlem, A., Hagberg, C. E., Muhl, L., Eriksson, U. & Falkevall, A. Imaging of neutral lipids by oil red O for analyzing the metabolic status in health and disease. *Nature protocols* **8**, 1149-1154, (2013).
148 Collins, T. J. ImageJ for microscopy. *BioTechniques* **43**, 25-30, (2007).
149 Venegas, V., Wang, J., Dimmock, D. & Wong, L.-J. Real-Time Quantitative PCR Analysis of Mitochondrial DNA Content. *Current Protocols in Human Genetics* **68**, 19.17.11-19.17.12, (2011).
150 Liberzon, A. *et al.* The Molecular Signatures Database (MSigDB) hallmark gene set collection. *Cell systems* **1**, 417-425, (2015).
151 Heinz, S. *et al.* Simple combinations of lineage-determining transcription factors prime cis-regulatory elements required for macrophage and B cell identities. *Molecular cell* **38**, 576-589, (2010).
152 Colombo, G. *et al.* A step-by-step protocol for assaying protein carbonylation in biological samples. *Journal of chromatography. B, Analytical technologies in the biomedical and life sciences* **1019**, 178-190, (2016).
153 Oki, S. *et al.* ChIP-Atlas: a data-mining suite powered by full integration of public ChIP-seq data. *EMBO reports* **19**, e46255, (2018).
154 Abhilash, L. & Sheeba, V. RhythmicAlly: Your R and Shiny-Based Open-Source Ally for the Analysis of Biological Rhythms. *Journal of biological rhythms* **34**, 551-561, (2019).
155 Hut, R. A. (https://www.euclock.org/results/item/circ-wave.html, 2015).

## ACKNOWLEDGEMENTS

We thank all members of Aguilar-Arnal and Orozco-Solis laboratories for helpful discussions and advice. We thank Alicia González-Manjárrez, PhD, from the Instituto de Fisiología Celular, UNAM, México, and Rudolf M. Buijs, PhD, from the Instituto de Investigaciones Biomédicas (IIB), UNAM, México, for their suggestions and comments on this research. We thank Victor Daniel Garzón Cortés, PhD, and the Unidad de Modelos Biológicos (UMB) at the IIB for their support with animal care and maintenance. We are thankful to Dr. Alfonso Leon-del-Rio laboratory at the IIB and particularly to Rafael Cervantes MSc, for kindly sharing reagents and equipment. We also thank the Microarray Unit at the Instituto Nacional de Medicina Genómica (INMEGEN, Mexico City) for assistance. We also thank to Alfonso González-Noriega, PhD, for his generous gift of equipment, reagents, and laboratory space. Research in LA-A lab was

supported by grants PAPIIT IA201717, IN210619 from Universidad Nacional Autónoma de México (UNAM), the Early Career Return Grant CRP/MEX16-05_EC from The International Center for Genomic Engineering and Biotechnology (ICGEB), Human Frontiers Science Program Young Investigators' Grant RGY0078/2017 and the National Council of Science and Technology (CONACyT) FORDECYT-PRONACES/15758/2020. RO-S lab was supported by CONACyT grants FC 2016/2672 and FOSISS 272757, and the INMEGEN (09/2017/I). QE-C acknowledges the reception of PhD fellowship from CONACyT, and a fellowship from DGAPA-PAPIIT IN210619. LM-V was a recipient of a postdoctoral fellowship from DGAPA-UNAM.

## AUTHOR´S CONTRIBUTION:

LA-A and RO-S conceived and designed the study. QE-C designed and conducted all experiments. LM-V, FB-P, IP-B, EC-V, PM-S, LA-A, RO-S, assisted with the *in vivo* experiments and tissue collection. MG-S and LA-A performed ChIP experiments. LM-V and MB-Z provided technical assistance. QE-C, LM-V, RO-S and LA-A analyzed and interpreted the data. QE-C and LA-A wrote the manuscript. All authors reviewed the manuscript and discussed the work.

## COMPETING INTERESTS:

The authors declare that the research was conducted in the absence of any commercial or financial relationships that could be construed as a potential conflict of interest.

# Figure Legends

**Figure 1. A $NAD^+$ chronotherapy at ZT11 improves the pathophysiology of diet-induced obesity.**

(**A**) Schematic diagram of the study design. Mice were fed either a normocaloric diet (CD) or a high-fat diet for 11 weeks. At week 8, a subgroup of high fat-fed mice was supplied a chronotherapy with $NAD^+$, consisting of a daily intraperitoneal injection of 50 mg/Kg of $NAD^+$ at ZT11 for three weeks (HFN). The rest of the mice were injected with vehicle (saline solution). (**B**) Weekly body weight (n = 17- 20 mice per group). Red arrow indicates the period of treatment with $NAD^+$ or saline at ZT11. (**C**) Hepatic $NAD^+$ content measured by HPLC along the day at the indicated times for all groups after the experimental paradigm (n = 5-8 biological replicates per time point, and 3 technical replicates). (**D**) Serum levels of insulin along the day at indicated times (n = 5 biological replicates per time point, and 2 technical replicates). AUC: area under the curve. (**E-H**) Glucose (E,F; GTT) and insulin (G,H; ITT) tolerance tests were performed at both the rest (ZT4) and the active (ZT16) period at the indicated days (10 and 20) after the beginning of treatments (n = 5-6 mice). AUC: area under the curve.
CD: Control diet fed mice; HF: High-fat diet fed mice; HFN: High-fat diet fed, $NAD^+$ treated mice at ZT11. Data represent mean ± SEM and were analyzed by two-way ANOVA using Tukey posttest, except when comparing AUC, where one-way ANOVA followed by Tukey's posttest was used. * $p < 0.05$, ** $p < 0.01$, *** $p < 0.001$. Points at ZT24 are duplicates of ZT0 replotted to show 24-h trends. Symbol key for comparisons: $^{*}$ CD vs HF; $^{+}$ CD vs HFN; $^{\#}$ HF vs HFN. Data from live mice were replicated in two independent experiments. See also complementary Figure S1.

**Figure 2. NAD⁺ chronotherapy ameliorates NAFLD**

(**A**) Representative hepatic histopathology. Upper panel: Oil-red-O stain (ORO). Lower panel: Hematoxilin/Eosin. Images were acquired at 20X optical magnification, and a detailed 100X digital magnification is shown (**B**) Quantification of ORO signal (arbitrary units). Signal for control mice was set to 1 (n = 3 biological and 3 technical replicates). (**C**) The length of lipid droplets was compared between groups (n = 3 biological and 3 technical replicates). (**D**) Distribution of hepatic triglyceride content across the day (left), and comparisons from all measurements (right) (n = 5 mice per time-point, with 2 technical replicates). (**E**) Protein carbonyl levels (PCO) in liver lysates were measured at the indicated times of day (n = 5 mice per time point, 2 technical replicates). AUC: area under the curve. (**F**) Relative mtDNA copies of mtCO1 respect to 18S DNA measured by Real-time PCR (n = 5 biological and 2 technical replicates). Inset area under the curve, content from CD group was set to 1. (**G**) Western blot from PPARγ1, 2 and CEBPα proteins in the mouse liver at the indicated times of day (ZT). GAPDH was used as loading control (WB was performed from 3 biological replicates with comparable results).

CD: Control diet fed mice; HF: High-fat diet fed mice; HFN: High-fat diet fed, NAD⁺ treated mice at ZT11. Data represent mean ± SEM and were analyzed by two-way ANOVA using Tukey posttest, except for bar graphs, where one-way ANOVA followed by Tukey's posttest was used. * $p < 0.05$, ** $p < 0.01$, *** $p < 0.001$. Symbol key for comparisons: $^{*}$ CD vs HF; $^{+}$ CD vs HFN; $^{\#}$ HF vs HFN. See also complementary Figure S2.

**Figure 3. Timed NAD⁺ supply induce a reprogramming of hepatic transcripts DE between day and night without altering the dynamics of clock proteins.**

(**A**) Heatmaps of 76 common differentially expressed (DE) transcripts between day (ZT6) and night (ZT18) in all groups. (**B**) Circadian protein expression of BMAL1, REV-ERBα, CRY1, and PER2 in the whole cell extracts from CD, HF, and HFN livers was determined by western blot. Tubulin or GAPDH were used as a loading control. (**C**) Quantification of western blots from n = 4 – 6 mice. Measurements were normalized to the loading control, and data from CD at ZT0 was set to 1. Means ± SEM are presented. ***p < 0.001, Two-way ANOVA; n.s.: non significative. Points at ZT24 are duplicates of ZT0 replotted to show 24-h trends. (**D**) Overlap of DE transcripts between day (ZT6) and night (ZT18) in all groups (FDR<0.05; fold change >1.3). (**E**) Heatmaps of distinct groups of DE transcripts between day (ZT6) and night (ZT18). Left: 322 transcripts DE exclusively in CD; center: 1327 DE exclusively in HF; right: 306 transcripts DE exclusively in HFN (**F**) Shared biological processes for DE transcripts between day and night from all groups. (**G**) Non-shared biological process for DE transcripts between day and night. CD: Control diet fed mice; HF: High-fat diet fed mice; HFN: High-fat diet fed mice, $NAD^+$ treated at ZT11.

**Figure 4. A $NAD^+$ chronotherapy at ZT11 corrects abnormal gene and protein expression from crucial molecular effectors of liver disease and triggers a specifc transcriptional signature.**

(**A, B**) Overlap (A) and heatmap (B) of DE genes when comparing CD-HF and HF-HFN groups either at day (ZT6) or ant night (ZT18) (n =3). (**C, D**) Functional annotation of CD-HF and HF-HFN shared genes at daytime (C) or nighttime (D). (**E**) Homer *de novo* motif discovery analyses from promoters of genes DE exclusively in the HF group. (**F, G**) Circadian protein expression of AKT, p-AKT(S473), AMPK and p-AMPK(T172) (F) or the mTOR pathway (G) in the whole cell extracts from CD, HF, and HFN livers was determined by western blot. Tubulin

or p84 were used as a loading control. Images represent 3-4 independent experiments. (**H, I**) Overlap (H) and heatmaps (I) of DE genes when comparing CD-HFN and HF-HFN groups either at day (ZT6) or at night (ZT18) (n =3) (**J**) Functional annotation of shared genes DE in analyses CD-HFN and HF-HFN at nighttime. (**K**) Homer *de novo* motif discovery analyses from promoters of genes whose expression is altered exclusively in the HFN group.
CD: Control diet fed mice; HF: High-fat diet fed mice; HFN: High-fat diet fed, $NAD^+$ treated mice at ZT11. See also Figure S3, S4 and Table S2.

**Figure 5. Time-of-day dependent response to $NAD^+$ treatment in obese mice determines the efficacy of the chronotherapy.**

(**A**) Weekly body weight (n = 15 mice per group). Red arrow indicates the period of treatment with $NAD^+$ or saline at ZT23. (**B**) Percent change in body weight between weeks 8 (just before treatment), and 11 (end of the treatment) (n =18-24 mice per group). (**C**) Weekly food intake from the indicated groups of mice is shown during three weeks before and after the $NAD^+$ treatment (n=33 mice). (**D**) Serum levels of insulin measured at ZT6 (day) and ZT18 (night) (n = 7-9 mice per time point). (**E**, **F**) Glucose (GTT) and insulin (ITT) tolerance tests were performed during the light period (ZT4) at the indicated days before (day 0) and after (day 20) $NAD^+$ treatment (n = 9-15 mice per group and day). (**G**) Relative delta comparing the differences between the area under the curves resulting from GTT and ITT in HF diet fed mice and the indicated groups of mice at days 0, 10 and 20 after $NAD^+$ treatment (**H**) Circadian serum triglyceride content (n = 9-10 mice per time point) (left), and direct comparisons from all measurements independently of ZT (right). (**I**) Representative hepatic histopathology. Upper panel: Oil-red-O stain (ORO). Lower panel: Hematoxilin/Eosin. Images were acquired at 20X optical magnification, and a detailed 100X digital magnification is shown (**J**) Bar graph

represents quantification of ORO signal in arbitrary units. Signal for control mice was set to 1 (n = 3 biological and 3 technical replicates). (**K**) The length of lipid droplets was compared between groups (n = 3 biological and 3 technical replicates) (**L**) Western blot of PPARγ1, 2 and CEBPα proteins in whole cell extracts from mouse liver at the indicated times of day (ZT). GAPDH was used as loading control. (**M**) Quantification of western blots from n = 4 - 5 mice. Measurements were normalized to GAPDH loading control, and data from CD at ZT0 was set to 1. *** p <0.001, two-way ANOVA with Bonferroni post-test.

CD: Control diet fed mice; HF: High-fat diet fed mice; HFN: High-fat diet fed, $NAD^+$ treated mice at ZT11; HFN23: High-fat diet fed, $NAD^+$ treated mice at ZT23. In the circadian plots, points at ZT24 are same as ZT0, replotted to show 24-h trends Data represent mean ± SE and were analyzed by two-way ANOVA using Tukey posttest, except when comparing AUC or hepatic stain, where one-way ANOVA followed by Tukey's posttest was used. * p <0.05, ** p <0.01, *** p <0.001; ns: non-significant. Symbol key for multiple comparisons: * CD vs HF; °CD vs HFN23; X HF vs HFN23. See also complementary Figure S5.

**Figure 6. Distinct impact of $NAD^+$ treatment at ZT11 versus ZT23 on hepatic nutrient and insulin sensing pathways.**

(**A**) Expression of AKT, p-AKT(S473), AMPK and p-AMPK(T172) along the day in the liver from mice treated with $NAD^+$ either at ZT11 (HFN) or at ZT23 (HFN23) was determined by western blot. GAPDH was used as a loading control (**B**) Quantification of western blots from n = 5 biological samples. Measurements were normalized to GAPDH loading control, and data from CD at ZT0 was set to 1. (**C**) Expression of proteins and phosphor-proteins in the mTOR pathway along the day in the liver from mice treated with $NAD^+$ either at ZT11 (HFN) or at

ZT23 (HFN23) was assessed by western blot. (**D**) Quantification of western blots from n = 5 biological samples. Measurements were normalized to p84 or GAPDH loading controls, and data from CD at ZT0 was set to 1. (**E-G**) RT-qPCR determined gene expression of rate-limiting and regulatory enzymes involved in mitochondrial (E) or peroxisomal (F) β-oxidation, and (G) ω-oxidation (n = 5 - 6 mice per data point).

CD: Control diet fed mice; HF: High-fat diet fed mice; HFN: High-fat diet fed, $NAD^+$ treated mice at ZT11; HFN23: High-fat diet fed, $NAD^+$ treated mice at ZT23. Data points at ZT24 are duplicates from ZT0, replotted to show 24-h trends. The data represent means ± SE. *p < 0.05, **p < 0.01, ***p < 0.001, Two-way ANOVA followed by Bonferroni's (B,D) or Tukey's (E-G) posttest. Symbol key for multiple comparisons: * HFN vs HFN23; # HF vs HFN. See also complementary Figure S6.

**Figure 7. $NAD^+$ resets the hepatic circadian clock**

(**A**) Circadian clock protein expression from liver whole cell extracts of obese mice treated with $NAD^+$ at ZT11 (HFN) or ZT23 (HFN23). Tubulin or GAPDH were used as loading control. (**B**) Quantification of western blots from n = 4 – 5 mice. Measurements were normalized to the loading control, and data from CD at ZT0 was set to 1 (n = 5 biological samples per data point) (**C**) RT-qPCR determined circadian clock gene expression in the liver (n = 5 - 6 biological replicates per data point) (**D**) RT-qPCR determined rhythmic expression of clock-controlled genes in the liver (n = 5 - 6 biological replicates per data point). (**E, F**) Chromatin immunoprecipitation (ChIP qPCR) was performed in the liver from mice at ZT6 or ZT18, using anti-BMAL1 antibodies. (n= 4 biological and two technical replicates). (**G**, **H**) RT-qPCR determined rhythmic expression of genes related to NAD+ metabolism (**G**) and genes regulating lipid metabolism (**H**) in the liver (n=5-6 mice per data point). BMAL1 ChIPs at ZT6 or

ZT18 were analyzed by performing qPCR on BMAL1 binding sites at selected regulatory elements of these genes.

CD: Control diet fed mice; HF: High-fat diet fed mice; HFN: High-fat diet fed, $NAD^+$ treated mice at ZT11; HFN23: High-fat diet fed, $NAD^+$ treated mice at ZT23. (B-D) Data points at ZT24 are duplicates from ZT0, replotted to show 24-h trends. The data represent means ± SE. *p < 0.05, **p < 0.01, ***p < 0.001, Two-way ANOVA followed by Tukey's posttest. See also complementary Figure S7.

**Figure 8. Time-of-day dictates efficiency of $NAD^+$ treatment of diet-induced metabolic disease through resetting the hepatic circadian clock and adjusting coordination between intracellular signaling and gene expression.**

(**A**) RT-qPCR from clock genes in the SCN at ZT0 and ZT12 (n=3 biological replicates and 2 technical replicates). (**B**) Representative double plotted actograms of locomotion measured using infrared sensors in a 12- hour light/12-hour dark cycle. (**C**) Average 24-hour activity profile from the indicated groups of mice. Average was calculated for five days after NAD+ treatment. n= 6-7 mice. (**D**) Food intake was measured over 24 hours (**E**) Average food intake during light phase (day) and dark phase (night). (**F**) $NAD^+$ bioavailability at a specific time of day resets the hepatic molecular clock. At ZT12, $NAD^+$ sustains the alignment of the hepatic molecular clock while reinforcing circadian oscillation in the activity of nutritional sensors such as AMPK, AKT or mTOR. Transcriptional responses are adjusted accordingly to suppress inflammation probably through inhibition of NF-κB transcription factor, and to increase amplitude in lipolytic gene expression with a peak during the active phase. Membrane trafficking and ULK activity are indicative of active autophagy as a specific response to $NAD^+$ treatment. At ZT0, increased $NAD^+$ in the liver resets the phase of the molecular clock,

imposing antiphase rhythms in clock gene and protein expression. This in turn inverts the phase of clock-controlled genes and uncouples transcriptional responses.

CD: Control diet fed mice; HF: High-fat diet fed mice; HFN: High-fat diet fed, $NAD^+$ treated mice at ZT11; HFN23: High-fat diet fed, $NAD^+$ treated mice at ZT23. (B-D) Data points at ZT24 are duplicates from ZT0, replotted to show 24-h trends. The data represent means ± SE. *p < 0.05, **p < 0.01, ***p < 0.001, Two-way RM ANOVA followed by Sidak's posttest. Symbol key for multiple comparisons: # HF vs HFN, X HF vs HFN23, $ HFN vs HFN23. See also complementary Figure S7.

Escalante-Covarrubias *et al.* **Figure 1**

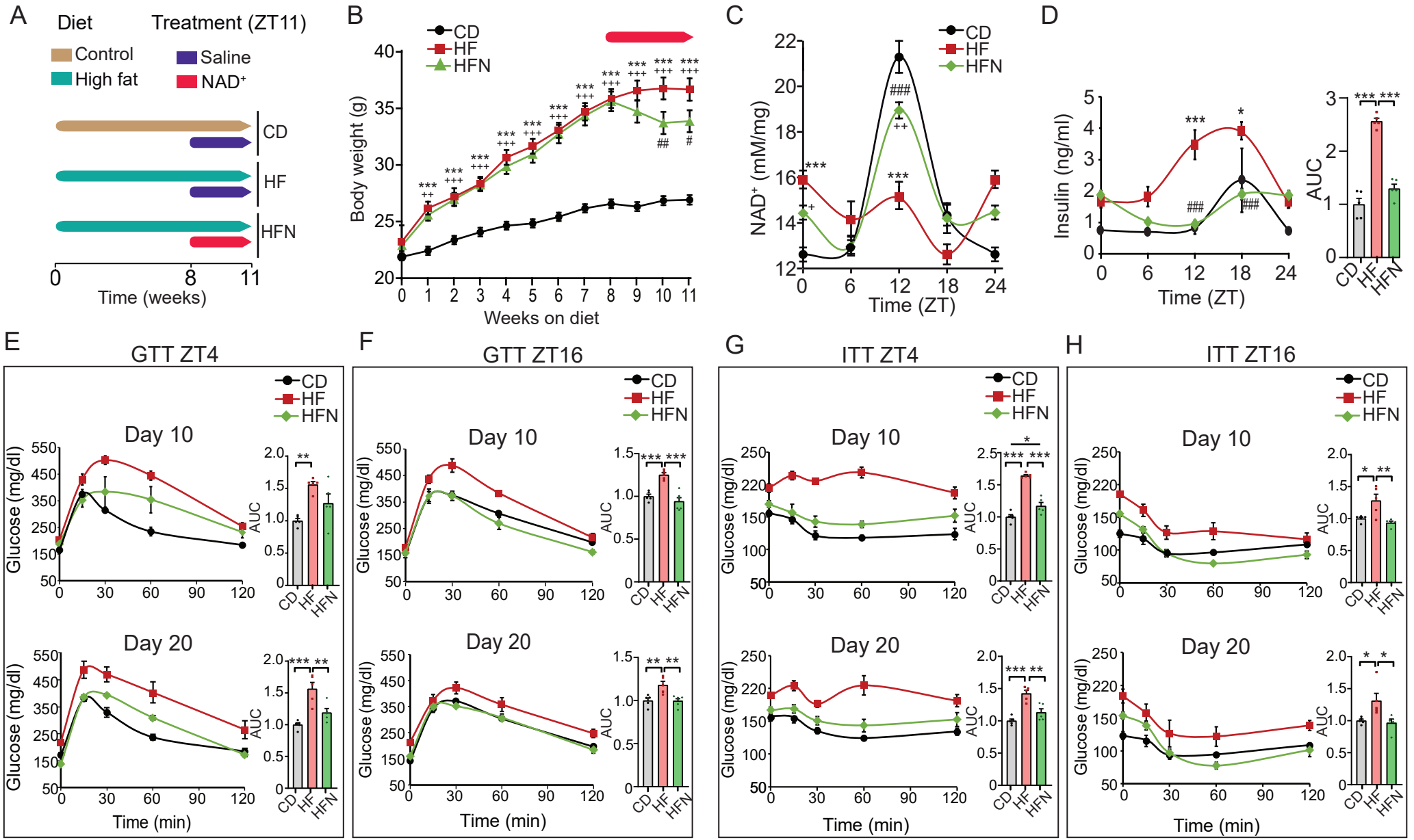

Escalante-Covarrubias *et al.* **Figure 2**

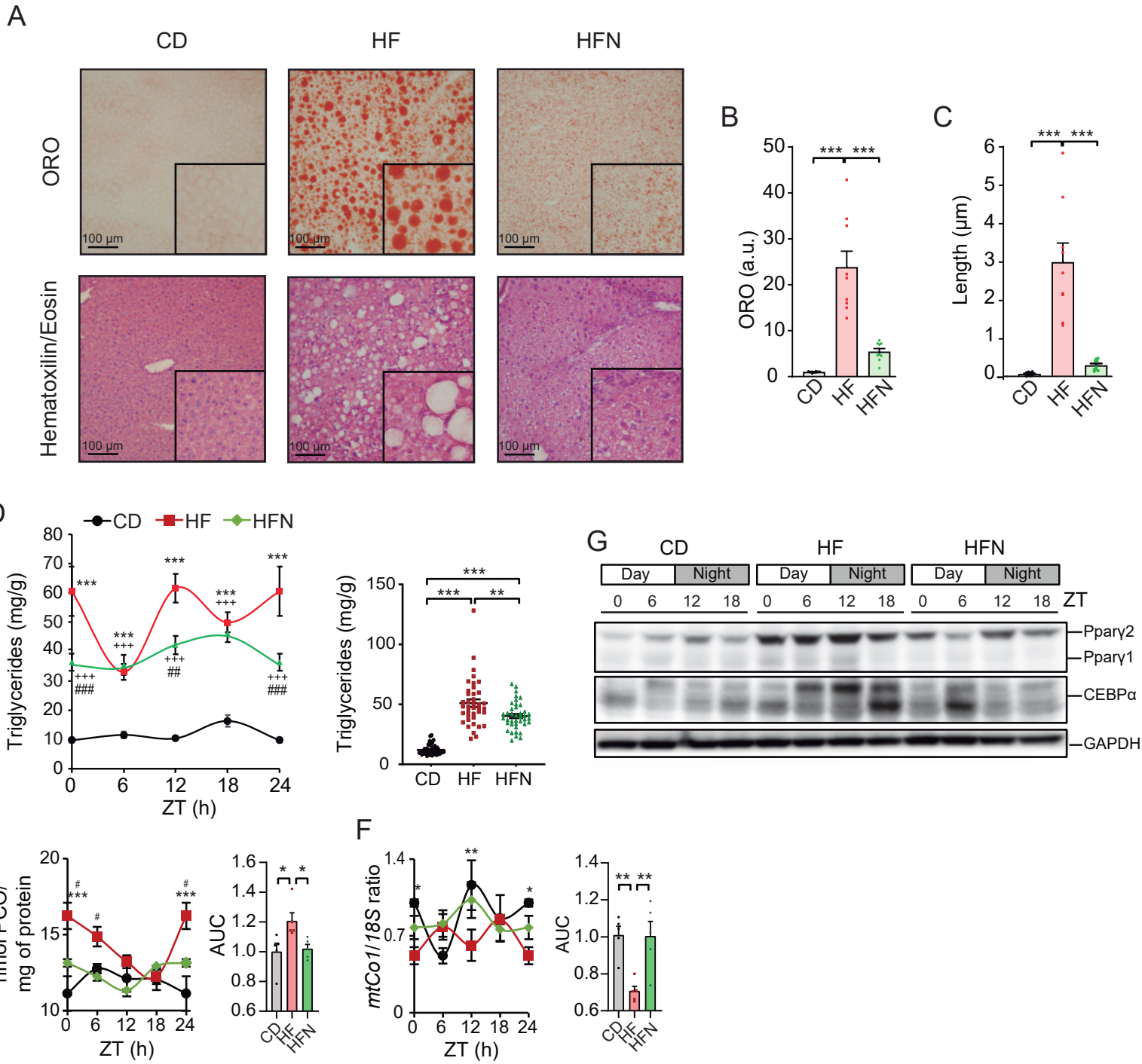

# Figure 3

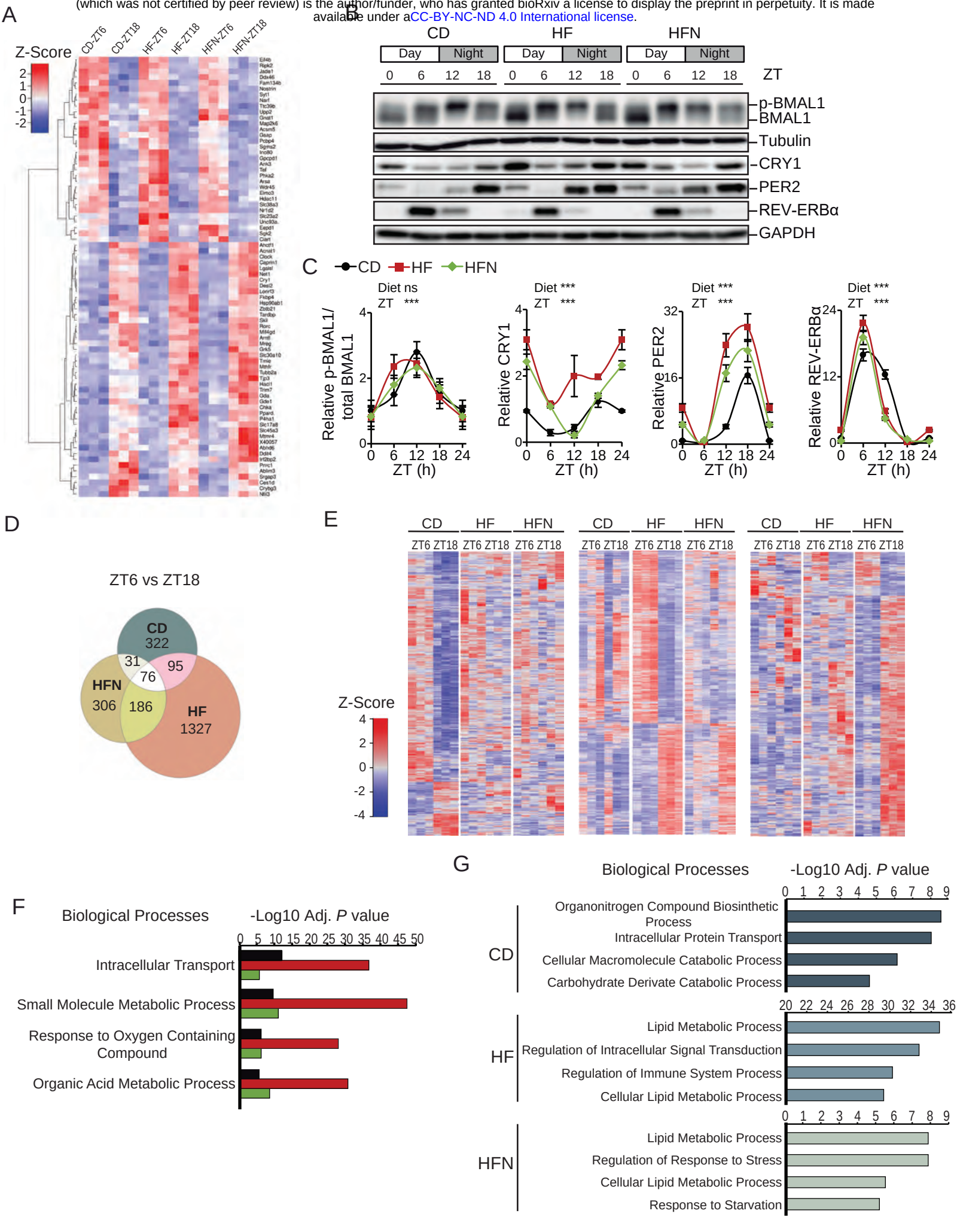

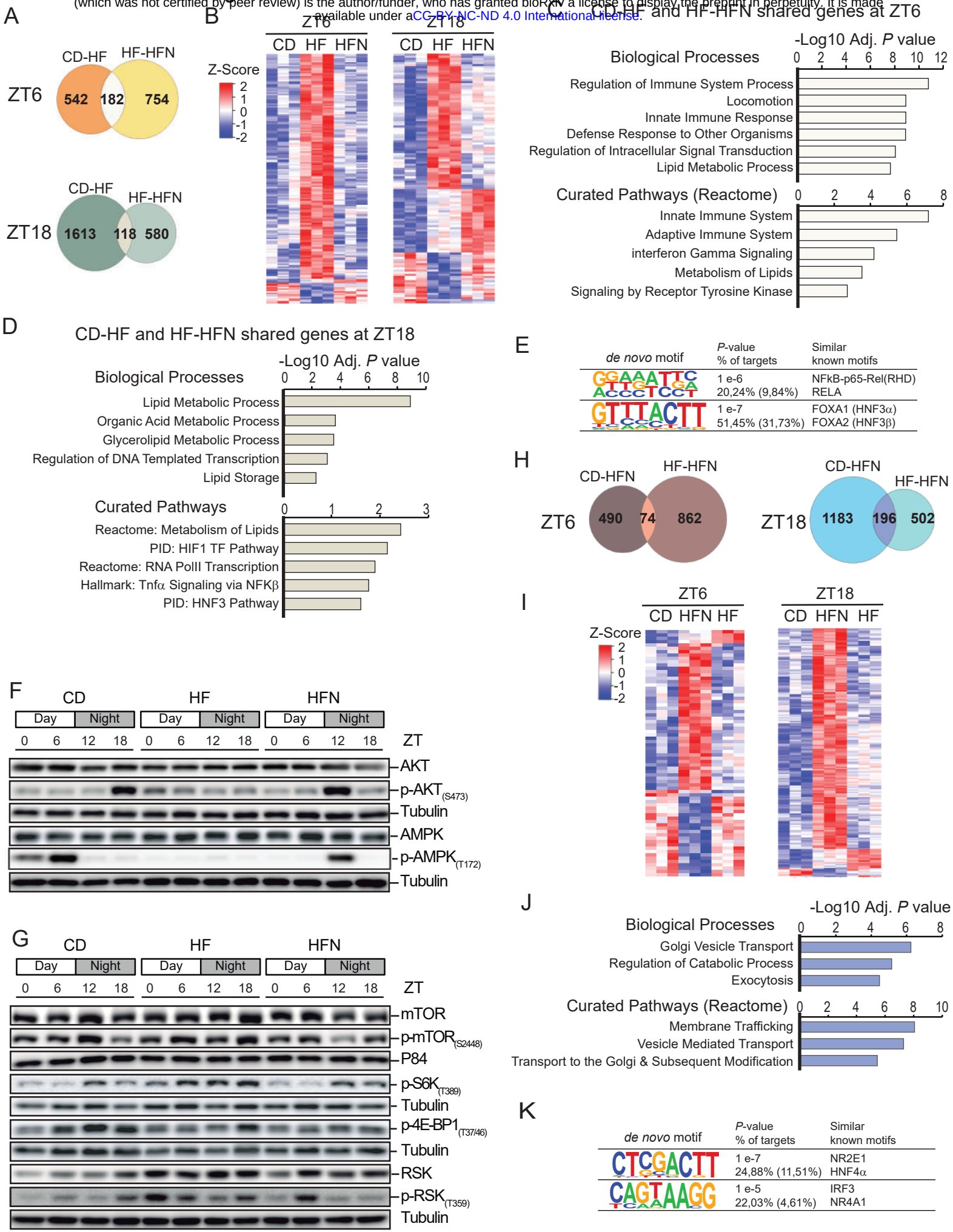

Escalante-Covarrubias *et al.* **Figure 5**

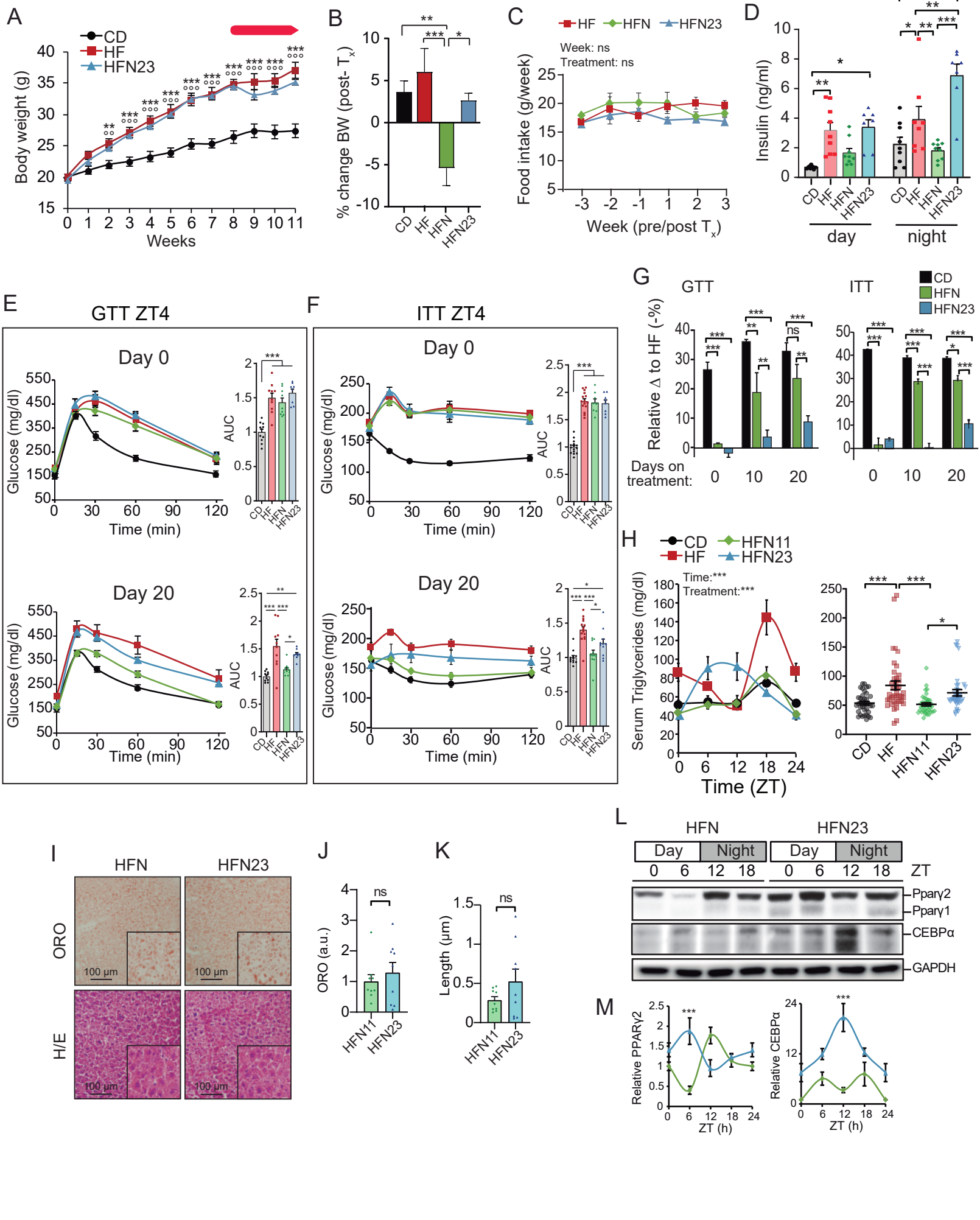

Escalante-Covarrubias *et al.* **Figure 6**

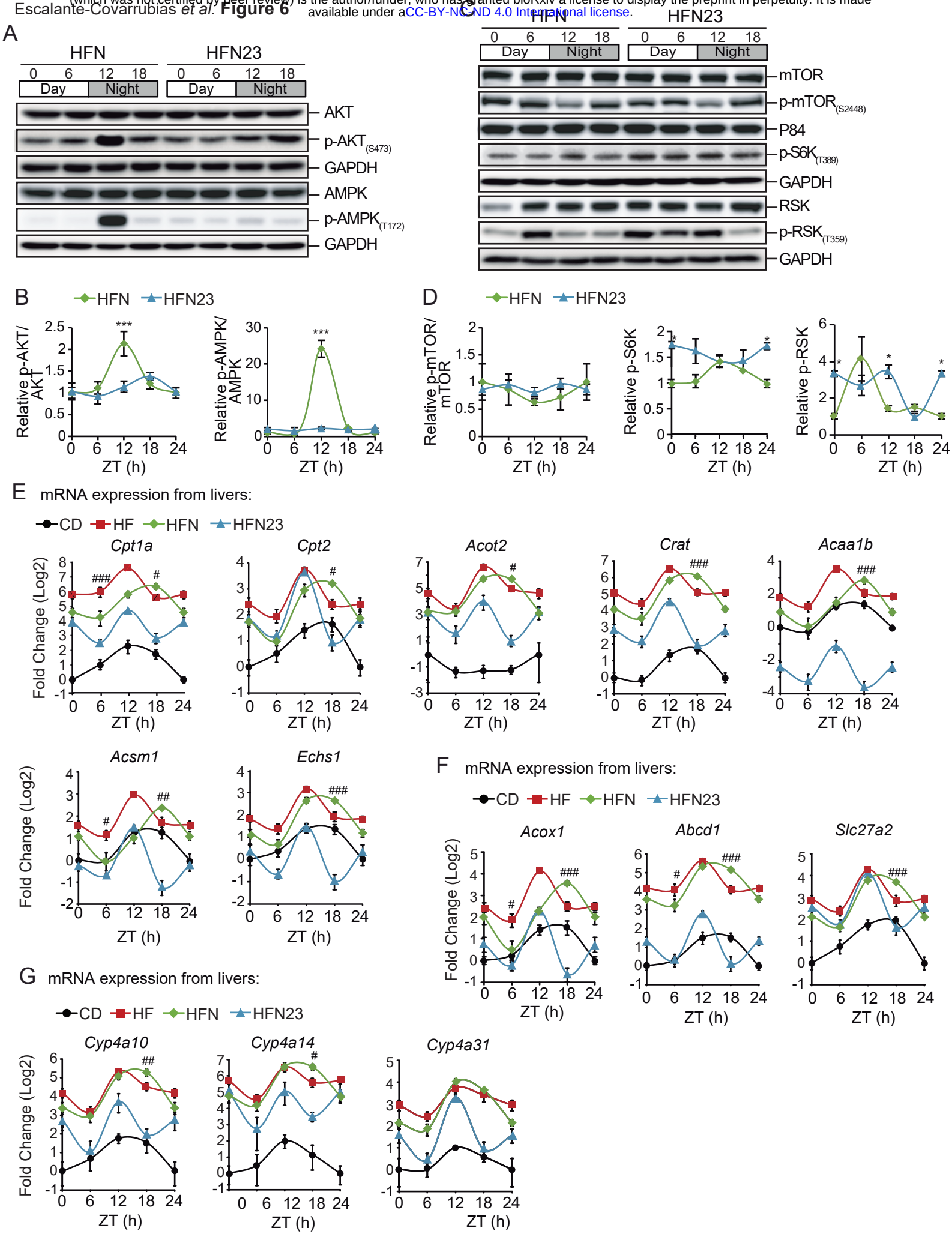

Escalante-Covarrubias *et al.* **Figure 7**